PHILOSOPHICAL TRANSACTIONS OF THE ROYAL SOCIETY A MATHEMATICAL, PHYSICAL & ENGINEERING SCIENCES

The Wake Instability in Viscoelastic Flow past Confined Circular Cylinders

Gareth H. McKinley, Robert C. Armstrong and Robert A. Brown

Phil. Trans. R. Soc. Lond. A 1993 **344**, 265-304
doi: 10.1098/rsta.1993.0091

The wake instability in viscoelastic flow past confined circular cylinders

By Gareth H. McKinley[1], Robert C. Armstrong[2] and Robert A. Brown[2]

[1] *Division of Applied Sciences, Pierce Hall, Harvard University, Cambridge, Massachusetts 01238, U.S.A.*

[2] *Department of Chemical Engineering, Massachusetts Institute of Technology, Cambridge, Massachusetts 01239, U.S.A.*

Contents

Laser Doppler velocimetry (LDV) and video flow visualization are used to investigate the creeping motion of a highly elastic, constant-viscosity fluid flowing past a cylinder mounted centrally in a rectangular channel. A sequence of viscoelastic flow transitions are documented as the volumetric flow rate past the cylinder is increased and elastic effects in the fluid become increasingly important. Velocity profiles clearly show that elasticity has almost no effect on the kinematics upstream of the cylinder, but that the streamlines in the wake of the cylinder are gradually shifted further *downstream*. Finite element calculations with a nonlinear constitutive model closely reproduce the evolution of the steady two-dimensional velocity field. However, at a well defined set of flow conditions the steady planar stagnation flow in the downstream wake is experimentally observed to become unstable to a steady, three-dimensional cellular structure. The Reynolds number at the onset of the flow instability is less than 0.05 and inertia plays little role in the flow transition. LDV measurements in the wake close to the cylinder reveal large spatially periodic fluctuations of the streamwise velocity that extend along the length of the cylinder and more than five cylinder radii downstream of the cylinder. Fourier analysis shows

Phil. Trans. R. Soc. Lond. A (1993) **344**, 265–304
Printed in Great Britain

that the characteristic spatial wavelength of these flow perturbations scales closely with the cylinder radius R. Flow visualization combined with LDV measurements also indicates that the perturbations in the velocity field are confined to the narrow region of strongly extensional flow near the downstream stagnation point. A second flow transition is observed at higher flow rates that leads to steady translation of the cellular structure along the length of the cylinder and time-dependent velocity oscillations in the wake. Measurements of the flow instability are presented for a range of cylinder sizes, and a stability diagram is constructed which shows that the onset point of the wake instability depends on both the extensional deformation of the fluid in the stagnation flow and the shearing flow between the cylinder and the channel.

1. Introduction

Operating limits are encountered in many industrial polymer processing applications at very low volumetric flow rates due to the onset of instabilities which are entirely absent in the corresponding flow of purely newtonian fluids (Petrie & Denn 1976). These instabilities develop at low Reynolds numbers and typically originate from the viscoelastic nature of the polymeric material. Over the past decade, significant progress has been made in understanding the spatial and temporal symmetries of viscoelastic flow instabilities by studying a number of simple test geometries that model individual elements of more complex commercial processing operations. Probably the best studied example to date is the transition from steady, two-dimensional creeping motion to a time-periodic, three-dimensional state that occurs in the flow of a highly elastic fluid between concentric circular cylinders. This Taylor–Couette instability is purely elastic in the sense that fluid inertia does not play a role in determining the onset of instability, and the flow transition occurs at a vanishingly small Taylor number. Instead, the relevant control parameter governing the onset of instability is the Deborah number which can be defined as a dimensionless ratio of an intrinsic time scale λ for the viscoelastic fluid (e.g. a characteristic polymer relaxation time) and a characteristic residence time $\mathscr{T}$ for the flow geometry under study. Above a critical value De_c, the steady, circular, base flow becomes unstable to a supercritical Hopf bifurcation and toroidal cells develop which propagate radially across the cylinder gap. Experimental studies (Muller *et al.* 1989), analytic predictions (Larson *et al.* 1990) and numerical calculations (Northey *et al.* 1991; Avgousti *et al.* 1991) have provided excellent agreement on the spatial form of the secondary flow, the onset point of the instability and the dependence on dimensionless gap width. The spatial and temporal structures of other low Reynolds number viscoelastic instabilities have also recently been documented in von Kármán swirling flows such as those experienced in cone-and-plate and parallel-plate rheometric devices (Magda & Larson 1988; McKinley *et al.* 1991*a*), and in Taylor–Dean rotational flows (Joo & Shaqfeh 1992). An extensive review of both elastic and inertial viscoelastic instabilities is given by Larson (1992).

Progress has been slower, however, in understanding the complex two- and three-dimensional geometries more typical of those encountered in commercial processing operations. Linear stability analyses are limited by the fact that, in most cases, no exact analytic solution exists for the steady base flow. Large-scale numerical simulations using simple quasilinear constitutive equations provide a qualitative

PHILOSOPHICAL TRANSACTIONS OF THE ROYAL SOCIETY A MATHEMATICAL, PHYSICAL & ENGINEERING SCIENCES

description of flow visualization experiments (cf. Walters & Webster 1982; Binding *et al.* 1987), and recently quantitative agreement with *steady-state* experimental data has become possible through the use of more realistic, but computationally more expensive, rheological models (Coates *et al.* 1992; Rajagopalan *et al.* 1992). To date, the stability of such flows at high Deborah numbers has been determined by direct experimental measurements. Simple flow visualization experiments provide an indication of globally unstable structures within a flow; however, visualization yields only qualitative information about the kinematics, such as the evolution of streamline shapes, and is generally limited to steady flows. In unsteady flows the particle tracks vary in time, and this can lead to apparent intersection of fluid streamlines (Binding *et al.* 1987). Semi-quantitative results may be extracted from the simple streak photographs obtained in flow visualization by manual measurements of the length and direction of individual particle tracks (Cable & Boger 1978). The spatial resolution of these measurements is limited, especially in flows with a wide dynamic range of velocities, such as flows involving recirculations, stagnation points or boundary layers. More accurate measurements of the spatial and temporal dynamics associated with viscoelastic flow transitions are imperative if experiments are to serve as a guide to future advances in numerical simulation of non-newtonian flows at high Deborah numbers.

Quantitative measurements of the velocity field are made by means of laser Doppler velocimetry (LDV). This technique has a wide dynamic range, is capable of resolving kinematic information on very localized length scales, and can yield both steady and time-dependent velocities. LDV is particularly useful in viscoelastic fluid mechanics since it is non-invasive to the local flow field being studied. More traditional measuring techniques, however, are known to be associated with well documented non-newtonian phenomena that lead to systematic errors in determination of kinematic data; common examples include the 'hole-pressure effect' in recess-mounted pressure transducers and the Uebler effect associated with the motion of tracer bubbles (Bird *et al.* 1987*a*). We used a three-colour, computer-controlled LDV system to document the sequence of flow transitions and nonlinear dynamics that develop in the entry flow of a highly elastic fluid through axisymmetric contractions (McKinley *et al.* 1991*b*). These measurements have shown that the macroscopic evolution of the vortex shape and size observed in earlier streak photographs (Boger 1987) was directly connected with a supercritical Hopf bifurcation to three-dimensional time-periodic motion near the re-entrant corner of the contraction. The time periodic nature of the flow was invisible to the streak photographs.

Here we report three-colour LDV measurements of the stability of viscoelastic flow past a circular cylinder. The experimental test geometry is shown in figure 1 and consists of a smooth circular cylinder of radius R mounted centrally in a long planar channel of height $2H$. Such geometric configurations ocur very commonly during extrusion operations, in which a polymer melt is forced under pressure past a die-forming element or *mandrell* that is typically held in place by cylindrical supports or *spiders* (Pearson 1985). A detailed investigation of this geometry also is a logical precursor to the study of more tortuous viscoelastic flows across arrays of cylinders that occur, for example, during matrix impregnation of fibrous composites (Skartsis *et al.* 1992) or flow through porous media (Georgiou *et al.* 1991).

The symmetry points (S_1, S_2) at the front and rear of the cylinder surface are *stagnation points* where polymer molecules will have large residence times in the

PHILOSOPHICAL TRANSACTIONS OF THE ROYAL SOCIETY A MATHEMATICAL, PHYSICAL & ENGINEERING SCIENCES

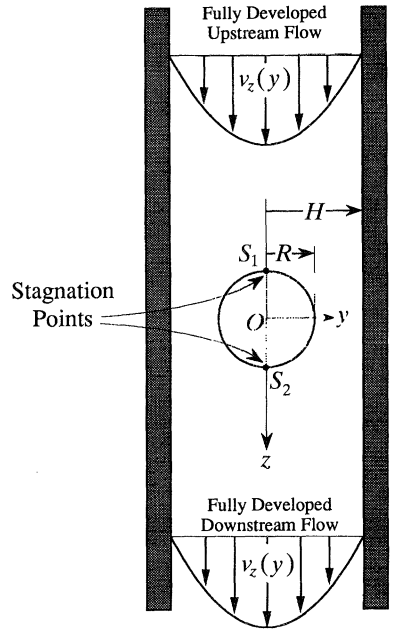

Figure 1. Viscolastic flow past a circular cylinder constrained in a planar slit. The cylinder of radius R is mounted centrally in the channel which has a half-height H. The cylinder–channel ratio is defined as $\beta = R/H$. A cartesian coordinate system is defined with its origin at the centre of the cylinder and the z-axis aligned with the flow direction.

vicinity of the cylinder, resulting in the development of large molecular extensions and significant elastic stresses. This stress boundary layer may result in significant modification of the fore/aft- and centreplane-symmetry in the velocity field that is predicted for the equivalent creeping flow of a newtonian liquid (Bairstow *et al.* 1922, 1923). These stresses can lead to the development of 'weld lines' in the wake of the obstacle, which, in turn, cause considerable degradation of the ultimate material properties of plastics extruded past submerged bodies (Tadmor & Gogos 1979).

If the average velocity of the fluid approaching the cylinder is denoted as $\langle v_z \rangle$, then a characteristic residence time for the geometry may be defined as $\mathscr{T} = R/\langle v_z \rangle$ and the Deborah number is then $De \equiv \lambda \langle v_z \rangle / R$. The ratio of the cylinder radius to the channel half-height is defined as the *cylinder–channel ratio*, $\beta \equiv R/H$. Recent studies of viscoelastic flow transitions in other complex geometries have shown that the resulting dynamic behaviour is extremely sensitive to relevant dimensionless geometric parameters, such as the plate aspect ratio in swirling flows (McKinley *et al.* 1991*a*), the contraction ratio in entry flows (McKinley *et al.* 1991*b*) and the dimensionless gap width in circular Couette flow (Shaqfeh *et al.* 1992). The experimental geometry used in this investigation is designed so that cylinders with varying radii can be inserted into the channel, and results are presented for cylinder-channel ratios in the range $0.16 \leqslant \beta \leqslant 0.50$.

The study of non-newtonian flow in this geometry has not been afforded the intense attention that has been focused in the past on viscoelastic entry flows. Yet, in many ways, this geometry is ideally suited as a test problem for viscoelastic fluid mechanics. Far upstream and downstream of the cylinder the flow is fully developed plane Poiseuille flow, but the complex fluid motion near the cylinder is a 'mixed flow' containing regions in the narrow gap between the cylinder and the walls where

shearing effects are dominant, and other regions near the upstream and downstream stagnation points where significant extensional effects occur. The relative contributions of these effects can be varied by considering different values of the cylinder–channel ratio β. These characteristics are analogous to those obtained in entry flows by varying the contraction ratio; however, in contrast to the contraction flow geometry, computational representations of this flow domain do not contain any geometric singularities, and hence the flow problem is more amenable to numerical simulations. For these reasons the analogous axisymmetric problem of viscoelastic flow around a sphere constrained in a cylindrical tube has recently been adopted as a benchmark problem for numerical computations (Hassager 1988; Crochet 1988; Lunsmann *et al.* 1993).

Early interest in viscoelastic flows around cylindrical and spherical objects arose from the central importance of standard flow measurement devices, such as hot wire anemometers and falling ball viscometers. Elasticity was found to perturb significantly the flow field around the body, and this resulted in alterations in the correlations of heat transfer and drag coefficients used to interpret the experimental measurements (see, for example, Leslie & Tanner 1961; Smith *et al.* 1967). Experimental studies of non-newtonian flow past spheres have been reviewed recently by Walters & Tanner (1992), and here we focus only on the less well studied case of flow past cylindrical bodies. Previous investigations may be grouped into two categories; studies of the creeping flow of highly elastic polymer solutions and melts past cylinders at high Deborah numbers but vanishingly small Reynolds numbers, and studies of higher speed flows of dilute polymer solutions at moderate values of De and Re.

Early analyses of non-newtonian creeping flow past a cylinder focused on two questions. What modifying influence does elasticity have on the velocity field, particularly the shape of the streamlines near the cylinder, and additionally how does the dimensionless drag coefficient C_D vary with increasing De? The first detailed theoretical analysis of viscoelastic flow past a cylinder was performed by Ultmann & Denn (1971) using the upper convected Maxwell (UCM) model. The Oseen approximation was used to linearize the momentum equation and by limiting the flow to small deformation rates the constitutive equation was reduced to the linear viscoelastic Maxwell model. This latter simplification is a much more severe limitation than the Oseen approximation, since the stagnation points on the cylinder surface lead to large velocity gradients and significant polymer deformations even at low Reynolds numbers. The approach has been criticized by Mena & Caswell (1974) and by Zana *et al.* (1975), since the approximation is not uniformly valid throughout the domain for any non-zero value of De and results in an over-specified set of boundary conditions.

The contribution of Ultmann and Denn is significant, however, because it indicated for the first time the possibility of a *change of type* in the visoelastic governing equations. The mathematical type of the equations was found to depend on the ratio of the mean cross-flow velocity to the velocity at which shear waves propagate through the elastic liquid. This dimensionless ratio can be expressed as the product of the Reynolds number and Deborah number; for $ReDe < 1$ the equation set is elliptic and the velocity solutions are smooth everywhere; however, for $ReDe \geqslant 1$, i.e. for velocities greater than the wave speed, the equation set becomes hyperbolic and discontinuities, or shocks, can propagate along the fluid streamlines (cf. Joseph & Saut 1986). Although Ultmann and Denn's final expression for the drag

PHILOSOPHICAL TRANSACTIONS OF THE ROYAL SOCIETY A MATHEMATICAL, PHYSICAL & ENGINEERING SCIENCES

coefficient is limited to small values of $ReDe$, they show that as elastic effects become important in the flow the drag coefficient decreases from the Stokes–Lamb solution expected for a newtonian fluid (Lamb 1932). The streamlines obtained by Ultmann and Denn indicated a large upstream displacement relative to the newtonian streamlines, even at very low values of De. Flow visualization experiments using dye-streaks to follow the streamlines around the cylinder also were presented for a newtonian fluid and a weakly viscoelastic carboxymethylcellulose solution. At a Deborah number of $De = 3.2 \times 10^{-3}$ the streamlines in the viscoelastic fluid were observed to be significantly shifted *upstream*. However, only one experimental observation was presented and no conclusions can be drawn about the effects of varying the Deborah number on the flow patterns.

Mena and co-workers carried out several investigations of creeping viscoelastic flow past cylinders and spheres. Mena & Caswell (1974) provided a rigorous matched asymptotic expansion valid for flows in the range $Re \ll 1$ and $De \ll 1$ for the Oldroyd-B constitutive equation. In direct contrast to the work of Ultmann and Denn, elasticity shifted the streamlines *downstream* by a distance of $O(De)$, and reduced the drag coefficient quadratically from the Stokes–Lamb solution for flow past a cylinder. Similar $O(De^2)$ reductions in the drag coefficients have been predicted theoretically for viscoelastic flow around a sphere (Leslie & Tanner 1961; Caswell & Schwarz 1962). Mena and Caswell's theoretical analysis agreed with experiments performed by Broadbent & Mena (1974) for flow around cylinders and spheres. Experimental measurements of the drag force confirmed a quadratic reduction in drag at low at De; however, flow visualization pictures showed no visually discernible streamline displacement upstream or downstream. In later experiments with cylinders, Manero & Mena (1981) used solutions of polyacrylamide in glycerine and water to span a wide range of De at low Re. For $De < 1$ a small downstream shift of the streamlines was observed; however, at higher Deborah numbers, $De > 1$, this shift was reversed and a larger upstream displacement of the streamlines could be seen. This initial downstream shift, followed by a larger upstream shift at high De, also was documented by Christiansen (1980) using dilute polyacrylamide solutions and two colour LDV measurements.

Walters and co-workers (Cochrane *et al.* 1981; Dhahir & Walters 1989) have investigated the constraining effects of side-walls by placing the cylinder in a square duct with a high cylinder–channel ratio of $\beta = 0.6$. The effects of fluid rheology were explored by using aqueous, shear-thinning solutions of polyacrylamide, a highly elastic, constant viscosity 'Boger fluid', and an aqueous solution of Xanthan gum (a rigid rod polymer). For each of these fluids, fluid elasticity was found to result in a reduction of the drag force on the cylinder; however, streak photographs again showed no difference between the streamlines observed for newtonian and non-newtonian fluids. Dhahir and Walters also investigated the effects of an asymmetric placement of the cylinder in the channel. Increasing the eccentricity of the cylinder placement reduced the drag force exerted on the cylinder while introducing a lift force normal to the flow and directed towards the closest wall.

The first numerical simulations to show the effects of elasticity on the flow characteristics were presented by Pilate & Crochet (1977) using a second-order-fluid model (Bird *et al.* 1987*a*). The authors found that for low Re and De the drag coefficient decreased from the newtonian value as observed in the experiments of Broadbent and Mena. Later calculations by Townsend (1980, 1984) using 2- and 4-constant Oldroyd fluid models supported these conclusions and found that at

PHILOSOPHICAL TRANSACTIONS OF THE ROYAL SOCIETY A MATHEMATICAL, PHYSICAL & ENGINEERING SCIENCES

moderate De, elasticity and shear-thinning effects caused a small downstream shift of the streamlines. The calculations of drag coefficient also agreed qualitatively with the earlier results of Pilate and Crochet.

Chilcott & Rallison (1988) performed time-dependent numerical calculations for unbounded creeping flow of a viscoelastic polymer solution past cylinders, cylindrical bubbles and spheres. The constitutive equation they used was based on a kinetic theory model for a dilute solution of macromolecules identified as non-interacting dumb-bells with finite extensibility. The numerical procedure allowed for the development of two-dimensional asymmetric or time-dependent solutions. However, for the range of parameters covered, no instabilities were encountered, and steady-state, symmetric solutions were obtained for all Deborah numbers up to $De = 16$. The calculations predicted high polymeric stresses, corresponding to large molecular extensions, that developed in three distinct regions: near the forward stagnation point; in the regions of high shear rate on either side of the cylinder, and in the long narrow wake downstream of the rear stagnation point. In this wake or 'birefringent tail' the highly extended dumb-bells are advected large distances downstream before relaxing fully. The development of very large extensional stresses in the wake of circular cylinders is supported by experimental measurements of intense flow-induced birefringence for both polymer solutions (Cressely & Hocquart 1980) and polymer melts (Mead 1987). The numerical results of Chilcott and Rallison again showed a small decrease in C_D for $De < 1$, followed by an increase above the newtonian value that asymptotically approached a constant plateau for $De \ll 1$. The use of a constitutive equation with a molecular interpretation in these calculations also demonstrated that, in addition to the relaxation time of the fluid, knowledge of the polymer chain extensibility is important in understanding viscoelastic flow near the cylinder. By varying the ratio of the fully extended to equilibrium length of the dumb-bell, and thus the degree of thickening in the extensional viscosity of the fluid, Chilcott and Rallison found they could alter the position of the asymptotic plateau in C_D to be either above or below the newtonian result. For highly extensible polymer molecules or for shear-thinning solutions the possibility of a 'negative wake' or velocity overshoot also was indicated.

Numerical simulations of the constraining effect caused by the proximity of channel walls have recently been performed by Carew & Townsend (1991). Once again the results indicated that both elasticity and shear-thinning effects caused a reduction in the drag coefficient but little change relative to the streamlines observed for creeping flow of a newtonian fluid. These authors also performed calculations for eccentric placements of the cylinder and were able to reproduce qualitatively the experimental findings of Dhahir and Walters indicating a normal or lift force on the cylinder directed towards the nearest wall.

The first detailed study of inertial effects in non-newtonian flow past cylinders was carried out by James & Acosta (1970). Heat transfer coefficients and drag coefficients of dilute polymer solutions were measured with extremely small cylinders constructed from standard hot wire anemometers over a range of Reynolds number $1 \leqslant Re \leqslant 100$. At a fixed Reynolds number, increasing the polymer concentration, and thus the fluid elasticity, reduced the heat transfer by up to 70% and increased the drag coefficient by a factor of three from the values obtained for newtonian fluids. Furthermore, the heat transfer from the cylinder became essentially independent of Re beyond a critical Reynolds number.

Visualization of the flow by James and Acosta, coupled with later LDV

PHILOSOPHICAL TRANSACTIONS OF THE ROYAL SOCIETY A MATHEMATICAL, PHYSICAL & ENGINEERING SCIENCES

measurements performed by Konuita *et al.* (1980) under similar conditions have shown that viscoelasticity results in a much broader and slower moving wake downstream of the cylinder and the development of a layer around the cylinder within which the fluid velocity is very low. It is the formation of this stagnant region and the increase in the effective size of the wake disturbance that results in the anomalous drag increase and reduction in heat transfer from the wire. Qualitative simulations of this phenomenon were discussed by Mizushina *et al.* (1975) and Townsend (1984), and very recently quantitative predictions of the changes in both the heat transfer coefficient and drag coefficient have been given by Hu & Joseph (1990) and Delvaux & Crochet (1990). Both of these latter numerical studies considered high Reynolds number flows of fluids modelled by the UCM constitutive equation and showed that the anomalous experimental correlations of transport properties corresponded directly to a change of type in the governing equations, as was first discussed by Ultmann & Denn. For flows with velocities greater than the shear-wave speed of the UCM model the calculations predicted large increases in the drag coefficient and corresponding decreases in the heat transfer coefficient, as observed by James & Acosta; plots of the flow streamlines for $ReDe \geqslant 1$ also reveal the development of a large region of slowly moving fluid near the cylinder, as seen in the experiments of Koniuta *et al.* (1980).

It therefore appears that the steady flow of viscoelastic fluids past cylinders is now well understood. At low Reynolds numbers the onset of elastic effects result in a small $O(De)$ downstream shift and a quadratic reduction in the drag coefficient, whereas at higher values of De fluid elasticity leads to a drag increase and, at least in the unbounded case, an upstream shift in the streamlines. As inertial effects become important in the fluid, the wake behind the cylinder becomes broader and a large region of slow moving fluid develops around the cylinder. Much less is known, however, about the stability of such flows. Several experimental studies with dilute polymer solutions have shown that the presence of trace amounts of polymers can delay the formation of the unsteady von Kármán vortex street that is observed in newtonian fluids beyond a critical value of the Reynolds number, and also significantly reduce the Strouhal frequency of vortex shedding (Usui *et al.* 1980; Kim & Telionis 1989). Similar viscoelastic restabilization of inertially driven instabilities is observed in other laboratory systems such as Taylor–Couette flow (Larson 1989; 1992). However, as discussed in the recent review by Larson, complex flows of highly elastic fluids may admit entirely new modes of instability with completely different spatial and temporal characteristics at moderate Deborah numbers and vanishingly small Re. To date, no experimental evidence has been presented for such instabilities in the wake of a circular cylinder. The early numerical studies discussed above were unable to obtain convergent steady-state solution fields for flow past a cylinder at moderate values of $De \approx 1$; however, this is due to difficulties associated with the numerical formulation of the problem, the so-called high Deborah number problem (cf. Keunings 1987; Crochet 1989), rather than to the onset of physically unsteady phenomena. The recent work of Chilcott & Rallison (1988) allowed for the possibility of asymmetric, or time-dependent two-dimensional solution fields; however, for the range of model parameters considered, symmetric steady-state solutions were obtained up to a $De = 16$. The appearance of three-dimensional instabilities has not been considered.

In this work we demonstrate that in highly elastic fluids a bifurcation from steady, two-dimensional, creeping flow to a new steady, three-dimensional motion occurs in

the cylinder wake at moderate values of the Deborah number and very small Reynolds numbers. A video-based flow visualization system is used to reveal the formation of a regularly spaced cellular structure in the wake of the cylinder, and three-colour LDV measurements are employed to determine quantitatively the three-dimensional velocity field. As the Deborah number is increased further, a second transition to a three-dimensional, time-dependent flow is documented corresponding to a translating cellular structure. The rheological properties of the viscoelastic fluid and the design of the experimental system used in this investigation are reviewed in §2. Both experimental and numerical studies of the evolution of the two-dimensional velocity field as De is increased are presented in §3; detailed experimental measurements of the spatial and temporal structure of the velocity field near the cylinder following the onset of three-dimensional flow follows in §4. The influence of varying the ratio of the cylinder radius to channel half-width β is discussed in this section. The connection of this work to experimental observations of other purely elastic flow instabilities in complex flow geometries is addressed in §5.

2. Experimental method

(*a*) *Flow geometry*

The flow geometry used in these experiments is shown schematically in figure 1. A cartesian coordinate system $\{x, y, z\}$ is defined with the origin at the centre of the cylinder, the z-axis aligned along the flow direction, the y-axis in the 'transverse' direction and the x-axis pointing in the 'neutral' direction along the cylinders axis of symmetry. The characteristic length scale is taken as the cylinder radius R, and non-dimensional coordinates are defined as $\xi \equiv x/R$, $\nu \equiv y/R$, $\zeta \equiv z/R$. Design specifications for the plexiglass test cell are discussed elsewhere (McKinley 1991), and the final internal dimensions of the rectangular channel are: length $\Delta z = 279.0$ mm, height $\Delta y \equiv 2H = 12.66$ mm, and width $\Delta x = 76.10$ mm. The cylinder is mounted half-way along the length of the channel, and the large entrance and exit lengths (*ca.* $22H$) ensure that the flow is fully developed as it approaches the cylinder. The aspect ratio of the channel cross-section is given by $\Delta x/\Delta y = 6.0$, which is designed to be as large as possible (within the constraint of maximum pump capacity) to minimize edge effects and ensure that the flow approaching the cylinder is approximately two-dimensional.

The circular cylinder itself consists of a single polished plexiglass rod that is held rigidly in place along the centreline of the channel by recessed holes in the side-walls of the flow cell. It is well-known that viscoelasticity tends to amplify slight asymmetries in this flow geometry (Cochrane *et al.* 1981; Walters 1985), and great care was taken to ensure that the mounting holes were centred to tolerances within $\delta y = \pm 0.025$ mm (*ca.* 0.001 inch). The dimensionless eccentricity associated with the cylinder mountings is therefore $\epsilon = \delta y/H \leqslant 4 \times 10^{-3}$. Because the viscoelastic test fluid used in this study is matched to have a refractive index very close to that of plexiglass, it is possible to transmit the focused laser beams of the LDV system through the front face of the flow cell and directly through the transparent cylinder without significant distortion. Velocity measurements were possible on both sides of the cylinder using this method.

The majority of the results presented here are for flow past a cylinder of radius $R = 3.188$ mm, such that the ratio of cylinder diameter to channel height is nom-

inally $\beta = 0.5$. A cylinder-channel ratio of $\beta = 0.5$ was originally proposed as an international benchmark for numerical simulations of viscoelastic flow in this geometry and the related axisymmetric problem of a sphere in a cylindrical tube (Hassager 1988); however, it has been suggested recently that smaller ratios should be considered in order to separate the competing influences of the constraining walls and the extensional flow near the stagnation point (Walters & Tanner 1992). The side-walls of the test cell used in these experiments can easily be removed to allow substitution of another cylinder with a different diameter. It is thus possible to explore the effect of varying β on the flow near the cylinder, and four different cylindrical rods with nominal ratios of $\beta = \frac{1}{2}, \frac{1}{3}, \frac{1}{4}$, and $\frac{1}{6}$ have been used in this work. The diameters of the cylinders were carefully determined with a digital micrometer at several positions along their lengths, and the actual cylinder–channel ratios are $\beta = 0.503 \pm 0.001$, $\beta = 0.337 \pm 0.001$, $\beta = 0.257 \pm 0.002$, and $\beta = 0.170 \pm 0.003$.

(*b*) *Laser Doppler velocimetry*

The LDV apparatus used in this research is a three-colour, six-beam system (TSI, Model 9100-12) that has been described in detail before (McKinley *et al.* 1992). The technique permits simultaneous non-invasive measurements of all three velocity components at a single point in the fluid where the six beams of laser light intersect. The spatial dimensions of this measuring volume are determined by the apertures and focal lengths of the focusing lenses and by the intersection angle and initial diameter of the laser beams. In the current configuration the measuring volume is ellipsoidal with dimensions of approximately 50 μm × 50 μm × 400 μm. The Doppler-shifted light that is scattered by particles in the flow is measured by three photomultipliers that are aligned in an off-axis, side-scatter configuration. The analogue voltage output from the photomultipliers is directed to three independent frequency trackers (DISA, Model 55N20/21) and a dual channel Spectrum Analyzer (Nicolet, Model 660B) to determine the Doppler frequency measured by each beam-pair. The digital output from each of these devices can be captured in the computer via standard RS232 and IEEE-488 interfaces respectively and steady and time-dependent velocity measurements in the range $0.1 \leqslant v \leqslant 100$ cm s^{-1} can be measured with accuracies of $\pm 1\%$. Acousto-optical Bragg cells are used to remove the directional ambiguities of the Doppler technique and permit the detection of any regions of reversing flow that may develop. The entire optical train is mounted on a computer-controlled, three-dimensional translating table (TSI, Model 9500) which enables point velocity measurements to be made throughout the flow geometry. In typical LDV applications involving air or water as test fluids it is common to add micrometre-sized seed particles as scattering sites; however, preliminary tests in the highly viscous polymeric liquids used in this work showed that no seeding is necessary because sufficient scattering particles are naturally suspended in the fluid.

In addition to point-wise measurements of the velocity field, the macroscopic characteristics of the flow are visualized using a CCD video-imaging system. A beam of laser light is passed through a cylindrical lens to form a narrow sheet of light as described by Cochrane *et al.* (1981), and this light sheet can then be used to illuminate various cross-sections of the plexiglass flow cell. Flow magnification factors in the range 7 to 30 are achieved by using a 35 mm macro lens and bellows rings assembly.

(c) *Test fluid rheology and dimensionless flow parameters*

The viscoelastic test fluid used in this study is a highly elastic 'Boger fluid' (Boger 1977) composed of 0.31% (by mass) polyisobutylene (PIB) dissolved in a viscous newtonian solvent of 94.86% (by mass) polybutene (PB) and 4.83% (by mass) tetradecane (C14). The test cell described in §2*a* is connected to a large flow loop containing approximately 60 gallons of the test liquid which is circulated by a variable-speed Moyno progressing-cavity pump.

The rheological properties of the fluid have been thoroughly characterized in dynamic, steady and transient shear flows over a range of temperatures (Quinzani *et al.* 1990). Master curves of the steady shear-flow material functions at a reference temperature of $T_0 = 25$ °C are shown in figure 2. The fluid has a zero-shear-rate viscosity $\eta_0 = 13.76$ Pa s and the viscosity remains almost constant over four decades of shear rate. Separate rheological measurements on the PB/C14 solvent show that it can be considered as a newtonian solvent with a constant viscosity of $\eta_s = 8.12$ Pa s. The first normal stress coefficient Ψ_1 is constant at low shear rates, with a zero shear-rate value of $\Psi_{1,0} = 8.96$ Pa s^2, but exhibits complex shear-thinning behaviour at higher shear rates. Although no direct measurements of the second normal stress coefficient for this fluid have been made, recent studies on other PIB Boger fluids have shown that $\Psi_2 \approx 0$ (Magda *et al.* 1991).

To obtain accurate estimates of the importance of elastic effects in the flow it is necessary to define an appropriate relaxation time for the fluid. In this work we define a shear-rate-dependent relaxation time in terms of the viscometric properties measured in steady shear flow as $\lambda(\dot\gamma) \equiv \Psi_1(\dot\gamma)/2\eta(\dot\gamma)$. In the limit of zero shear-rate this definition yields a maxwellian relaxation time of $\lambda_0 = 0.324$ s, and also takes into account the gradual decrease in the first normal stress coefficient that is observed at moderate shear-rates for all Boger fluids. The volumetric flow rate (Q) through the geometry is used to define an average velocity in the channel as $\langle v_z \rangle \equiv Q/\Delta x \Delta y = Q/24H^2$, and a characteristic residence time for polymer molecules flowing near the cylinder is $\mathscr{T} \equiv R/\langle v_z \rangle$. The Reynolds number and the Deborah number for this problem are then defined respectively by

$$De \equiv \lambda(\dot\gamma)\langle v_z \rangle / R \tag{1}$$

and

$$Re \equiv 2\rho \langle v_z \rangle R/\eta(\dot\gamma). \tag{2}$$

In equation (2) we have indicated that, for polymeric fluids in general, the viscosity may also be a shear-rate-dependent quantity; however, for the Boger fluid used here η remains essentially constant at the zero-shear-rate value given above. Many other workers report Deborah numbers based on the constant relaxation time obtained from zero-shear-rate viscometric properties. Therefore, we also report these values in the tables of critical conditions below; however, as we discuss in §3, in general the zero-shear-rate Deborah number, $De_0 \equiv \lambda_0 \dot\gamma$, significantly over-predicts the magnitude of elastic effects in a Boger fluid.

(d) *Constitutive model*

Quinzani *et al.* (1990) showed that simple quasilinear models, such as the Oldroyd-B fluid model (Oldroyd 1950), are insufficient to describe the deformation-rate-dependent rheological properties of the PIB test fluid, and it is necessary to use both a spectrum of relaxation times and nonlinear constitutive equations. Numerical

PHILOSOPHICAL TRANSACTIONS OF THE ROYAL SOCIETY A MATHEMATICAL, PHYSICAL & ENGINEERING SCIENCES

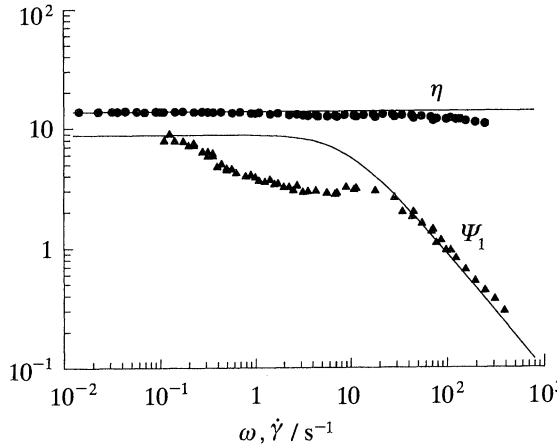

Figure 2. Master curves for the viscometric properties of the 0.31 % (by mass) PIB/PB/C14 Boger fluid at $T_0 = 25$ °C: (●) shear viscosity η (Pa s) and (▲) first normal stress coefficient Ψ_1 (Pa s^2). Also shown by the solid lines are the predictions of the Chilcott–Rallison model (equation (3)) with $c = 0.695$ and $L = 12$. $\eta_0 = 13.76$ Pa s, $\eta_s = 8.12$ Pa s, $\Psi_{10} = 8.96$ Pa s^2.

simulations with such multimode models are just beginning (cf. Rajagopalan *et al.* 1992); however, the calculations are currently very expensive. To decrease the size of the equation set, but retain at least a semiquantitative description of the shear-rate dependence in the first normal stress coefficient that is observed in Boger fluids, we have used the single-mode nonlinear constitituve equation introduced by Chilcott & Rallison (1988). The PIB macromolecules are considered as a dilute solution of non-interacting dumb-bells with dimensionless concentration c, dissolved in a newtonian solvent of viscosity η_s. The two beads of the dumb-bell are connected by a nonlinear elastic spring with a finite maximum extensibility L, which represents the ratio of the fully extended length of the dumbbell to the RMS length at equilibrium. A constitutive equation for the polymeric contribution to the fluid stress $\boldsymbol{\tau}_p$ is obtained by eliminating the dyadic product of the end-to-end vector from the original equations of Chilcott and Rallison to obtain (in the notation of Quinzani *et al.*) the following expression

$$\lambda_1 \boldsymbol{\tau}_{p(1)} + \boldsymbol{\tau}_p \left[Z - \lambda_1 \frac{D \ln Z}{Dt} \right] = -\eta_p Z \dot{\boldsymbol{\gamma}}, \tag{3}$$

where

$$Z \equiv (L^2 - (1/nkT) \operatorname{tr} \boldsymbol{\tau}_p)/(L^2 - 3)$$

and $\operatorname{tr} \boldsymbol{\tau}_p$ is the trace of the stress tensor, λ_1 is a time constant for the model, T is the temperature and n is the number density of dumb-bells in solution. It can be shown that the polymeric contribution to the viscosity is $\eta_p = nkT\lambda_1$. The solvent is newtonian with $\boldsymbol{\tau}_s = -\eta_s \dot{\boldsymbol{\gamma}}$ and the total stress tensor for the fluid is given by summing the separate contributions from the solvent and polymer as $\boldsymbol{\tau} \equiv \boldsymbol{\tau}_s + \boldsymbol{\tau}_p$.

In the limit $L \to \infty$, the dumb-bells become infinitely extensible and equation (3) simplifies to the upper-convected Maxwell model; the constitutive equation for the total stress tensor $\boldsymbol{\tau}$ is then equivalent to the Oldroyd-B model (Bird *et al.* 1987*b*). Chilcott & Rallison provide analytic expressions for the material functions obtained from (3) for finite L and show that the model correctly mimics numerous aspects of Boger fluid rheology including a constant viscosity, a shear-rate-dependent first

normal stress coefficient and a zero second normal stress coefficient. The results of fitting the three Chilcott–Rallison model parameters η_s, c, and L to the viscometric data for the 0.31% (by mass) PIB Boger fluid are shown in figure 2. The dimensionless concentration is found from the zero-shear-rate viscosity $\eta_0 \equiv \eta_s + \eta_p = \eta_s(1+c)$ as $c = 0.69$; for moderate or large values of L, the time constant λ_1 is determined directly from the zero-shear-rate material properties as $\lambda_1 \approx \Psi_{1,0}/2(\eta_0 - \eta_s) = 0.794$ s. The single remaining model parameter L is then determined by fitting the shear-rate-dependent form of the first normal stress coefficient. For this 0.31% (by mass) PIB Boger fluid we find that the asymptotic form of $\Psi_1(\dot\gamma)$ at high shear-rates is best modelled by a relatively low value of the extensibility, $L = 12$. Chilcott and Rallison suggest typical parameter ranges for Boger fluids of $0.3 \leqslant c \leqslant 0.7$ and $3 < L \leqslant 20$, in good agreement with our findings. By using the definition in (1), the shear-rate-dependent Deborah number for the Chilcott–Rallison model is given as

$$De(\dot\gamma) = \frac{1}{4}\frac{L^2}{\lambda_1 \dot\gamma}\frac{c}{(1+c)}\left\{-1+\sqrt{\left[1+\frac{8(L^2-3)(\lambda_1\dot\gamma)^2}{L^4}\right]}\right\}, \tag{4}$$

where the magnitude of the deformation rate is $\dot\gamma \equiv \langle v_z\rangle/R$.

In addition to capturing the shear-thinning behaviour in $\Psi_1(\dot\gamma)$, the Chilcott–Rallison model predicts a large but bounded extensional viscosity $\bar\eta$ in steady extensional flows and removes the singular behaviour encountered at critical extension rates with quasilinear constitutive equations, suh as the Oldroyd-B model (Bird *et al.* 1987*a*). This is important in numerical simulations of viscoelastic flow past cylinders and spheres since fluid near the stagnation points experiences strong extensional deformations. The model parameters determined in (3) predict a maximum planar extensional viscosity of $\bar\eta_1 \approx 120\eta_0$ at large extension rates.

Finally it should be noted that although the model of Chilcott and Rallison incorporates many aspects of Boger fluid rheology, it only contains a single time constant for the fluid. In the limit of infinitesimal deformation rates the constitutive equation reduces to the linear viscoelastic Jeffreys model, and thus cannot accurately describe the gradual frequency dependence of the linear viscoelastic material functions (η', η'') that is observed in Boger fluids. It has also been shown that a quantitative description of the intermediate plateau behaviour in the experimental measurements of the first normal stress coefficient $\Psi_1(\dot\gamma)$ can be achieved through the incorporation of multiple relaxation modes (Quinzani *et al.* 1990).

3. Steady viscoelastic flow past a cylinder

We present in this section the results of experimental measurements and numerical simulations that document the evolution of the steady, two-dimensional velocity field near the circular cylinder as the volumetric flow rate, and thus $De(\dot\gamma)$ are slowly increased.

(*a*) *Newtonian flow past a confined cylinder*, $De \ll 1$

Far upstream and downstream of the cylinder, the fluid motion in the rectangular slit should be a fully developed rectilinear shear flow. In particular, for the creeping motion of a constant-viscosity Boger fluid in an *infinitely* wide channel we expect a plane Poiseuille flow with a parabolic profile and a maximum velocity on the centreline of $v_z = \frac{3}{2}\langle v_z\rangle$. However, the velocity must also vary in the 'neutral' x-direction, because of the finite extent of the experimental apparatus and the no-slip

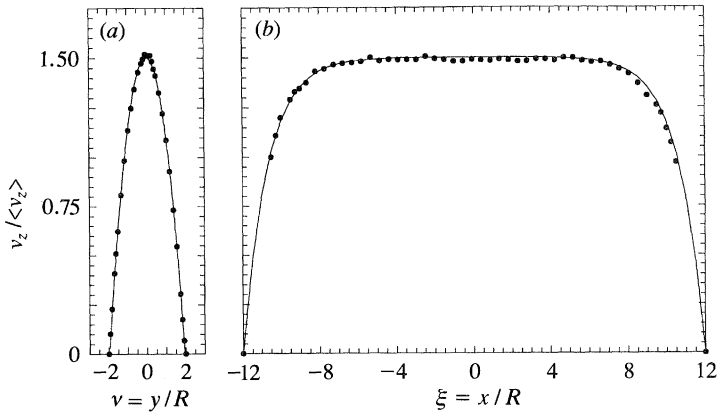

Figure 3. Profiles of the axial velocity component in a rectangular channel with aspect ratio 6:1. (*a*) Parabolic dimensionless velocity profile $v_z(y)/\langle v_z\rangle$ in transverse direction, and (*b*) flat velocity profile $v_z(x)/\langle v_z\rangle$ across width of channel. The solid lines are calculated with an analytical, infinite-series solution to the equations of motion. $De = 0.7$, $Re = 0.0057$, $(\nu, \zeta) = (0, -10)$.

boundary conditions at the end-walls. Significant three-dimensional effects have been observed in earlier flow visualization experiments of viscoelastic flow past cylinders in ducts with almost square cross-sections (Dhahir & Walters 1989; Georgiou *et al.* 1991). We have aimed to minimize these edge effects by designing the test cell with a higher aspect ratio of $\Delta x/\Delta y = 6.0$. Profiles of the normalized axial velocity $v_z(\xi, \nu)/\langle v_z\rangle$ in the rectangular channel are shown in figure 3 at a dimensionless position of $\zeta = -10$, i.e. ten cylinder radii upstream of the cylinders midpoint. The velocity in the transverse y-direction is shown in figure 3*a* and has the characteristic parabolic profile with a maximum value of $v_z/\langle v_z\rangle \approx 1.5$ at $\nu = 0$. The axial velocity across the width of the channel is shown in figure 3*b* and rises very rapidly from zero at either end-wall to an approximately constant profile across the central two-thirds of the channel for dimensionless x positions, $-8 \leqslant \xi \leqslant 8$. Also shown in figure 3 are dimensionless velocity profiles calculated with an infinite-series solution of the Stokes equations for creeping flow of a newtonian fluid in a rectangular channel. The agreement is excellent between the LDV measurements and the analytic solution. The average velocity at these flow conditions is $\langle v_z\rangle = 1.47$ mm s^{-1}, and the small fluctuations observed in the experimental data points shown in figure 3*b* indicate the magnitude of the minimum resolvable velocity difference (± 0.04 mm s^{-1}) that can be detected with the LDV system.

The evolution of the velocity field around the cylinder at low *De* is summarized in figure 4. The velocity profile is parabolic far upstream ($\zeta = -10$), and flattens as the fluid approaches the cylinder ($\zeta = -3$). Off-centre maxima develop at $\zeta = -2$, and the velocity attains a maximum value on the symmetry plane, $\zeta = 0$. At this point the velocity profile on each side of the cylinder is again parabolic, as expected for such an inertialess flow, with a maximum velocity of $v_z/\langle v_z\rangle = 3.0$ at the points $\nu = \pm 1.5$. The velocity profiles are symmetric downstream of the cylinder, and the flow rapidly returns to the parabolic profile within a distance of five cylinder radii from the rear stagnation point.

LDV measurements of the axial velocity in the planar stagnation flow near the cylinder are presented in figure 5. Far upstream and downstream of the cylinder the normalized velocity along the channel centreplane $(\xi, \nu) = (0, 0)$ has a maximum

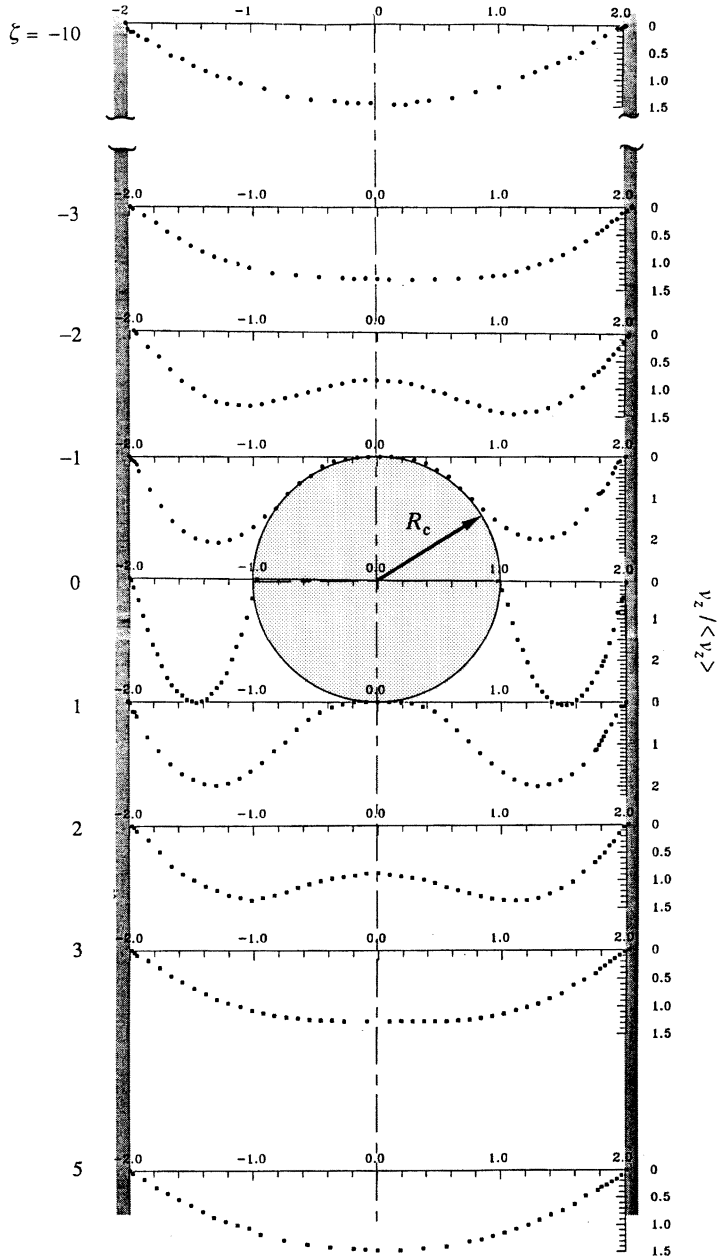

Figure 4. Transverse velocity profiles of the dimensionless axial velocity $v_z/\langle v_z\rangle$ showing evolution of the velocity field for the creeping flow of the Boger fluid past a circular cylinder at flow conditions of $De = 0.07$ and $Re = 0.0003$.

value of $v_z/\langle v_z\rangle = 1.5$. As the fluid approaches the cylinder the velocity decreases very rapidly; figure 5 shows that the influence of the cylinder only extends a distance of about four cylinder radii from the upstream and downstream of the stagnation points S_1 and S_2 located at $\zeta = \pm 1$.

Numerical solutions for the two-dimensional, inertialess flow of a viscoelastic fluid past a cylinder in a planar channel with $\beta = 0.5$ have been obtained using the finite

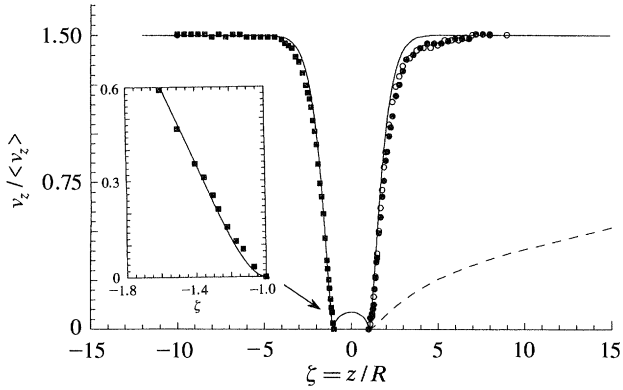

Figure 5. Centreline axial velocity in the planar stagnation flow near the cylinder at $De = 0.07$: (●) LDV measurements in flow geometry with $R = 6.37$ mm, and 10:1 aspect ratio; (○) LDV measurements in flow geometry with $R = 3.188$ mm and 6:1 aspect ratio. (——) Two-dimensional finite element solution for $\beta = 0.5$; (– – –) Lamb–Oseen solution for slow flow past an unbounded cylinder. $(\xi, \nu) = (0, 0)$.

element code developed by Lunsmann (1992). The numerical formulation employed in this work has been shown to be convergent with mesh refinement for the Oldroyd-B and Chilcott–Rallison models (Lunsmann *et al.* 1993), and has been employed to provide benchmark solutions for studies of the equivalent axisymmetric problem of a sphere falling in a tube (Walters & Tanner 1992). The centreline velocity profiles obtained numerically at $De = 0$, and $Re = 0$ are shown in figure 5 by the solid lines. The agreement between the numerical computations and the LDV measurements is extremely good in both the upstream and downstream stagnation flow. The inset figure shows an expanded view of the velocity profile near the upstream stagnation point with LDV measurements obtained at equally spaced intervals of 160 μm ($0.05R$). The maximum discrepancy shown in figure 5 is approximately 7% and occurs in the downstream wake of the cylinder at distances of $3.0 \leqslant \zeta \leqslant 4.0$. The reproducibility of this effect was investigated with LDV measurements that were performed at the same De in two separate flow geometries; one with a cylinder radius $R = 3.188$ mm and a 6:1 cross-sectional aspect ratio (depicted by the solid symbols in figure 5) and a second test cell with a cylinder radius of $R = 6.370$ mm and an aspect ratio of 10:1 (hollow symbols in figure 5). The two data sets are self-consistent and both show the same, small 7% deviation from the numerical calculations. The origin of this discrepancy is unclear, but it seems unlikely to be due to the finite cross-sectional area of the experimental geometry or to be an inertial effect for the very small values of $Re < 0.001$ attained in the experiments. The data in figure 5 do show a slight asymmetry which should not be present for the creeping flow of a fluid past a cylinder at zero Deborah number, and it thus appears that the small, but finite elasticity present in the experimental fluid contributes to this small effect. The theoretical studies discussed in §1 suggest that elasticity results in an $O(De)$ downstream shift in the streamlines (Mena & Caswell 1974), and subsequent numerical calculations with the Oldroyd-B model at $De = 0.1$ also show a very small downstream displacement of about 2% in the centreline velocity profile. However, this shift is insufficient to describe quantitatively the experimental data shown in figure 5. It seems most probable that the small discrepancy arises from viscoelastic behaviour not modelled by the single mode constitutive models; examples may be

PHILOSOPHICAL TRANSACTIONS OF THE ROYAL SOCIETY A MATHEMATICAL, PHYSICAL & ENGINEERING SCIENCES

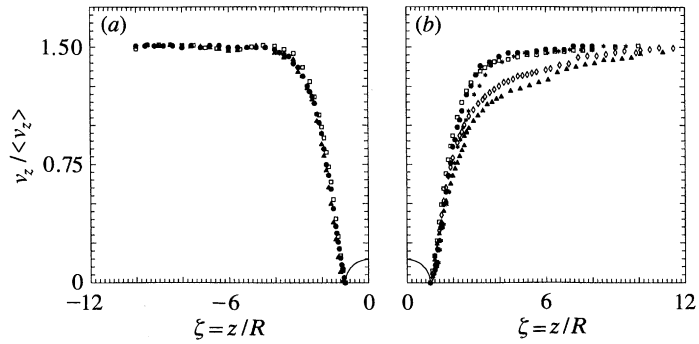

Figure 6. Evolution of the axial velocity profiles $v_z/\langle v_z\rangle$ along the channel centreplane ($y = 0$) with increasing De: (a) upstream of the cylinder; and (b) in downstream wake of the cylinder. $(\xi, \nu) = (0, 0)$. In (a) $De = 0.074$ (●), 0.41 (□) and 0.85 (▲). In (b) $De = 0.074$ (●), 0.19 (□), 0.35 (∗), 0.52 (◇) and 0.69 (▲).

the complex shear-thinning observed in $\Psi_1(\dot{\gamma})$ or the spectrum of relaxation times present in this Boger fluid (Quinzani *et al.* 1990).

The constraining effect of the channel walls is emphasized by the broken curve in figure 5 that shows the normalized velocity profile calculated from the Lamb–Oseen solution for the slow flow of a newtonian fluid past a circular cylinder. In an unbounded fluid, reductions in the free stream velocity occur out to distances $\zeta \sim 1/Re$; however, the presence of channel walls deter the fluid from being forced radially outwards by the cylinder and result in a much more rapid decrease in the velocity near the stagnation point. Consequently much larger extension rates are observed experimentally and calculated numerically near the stagnation points in the confined geometry.

(*b*) *Effects of elasticity on the velocity field*, $De \sim 1$

As the Deborah number of the flow past the cylinder is increased, elastic effects result in a progressive modification to the velocity field around the cylinder. Profiles of the normalized axial velocity along the centreplane in the front and rear stagnation flows near the cylinder are shown in figure 6 to demonstrate this effect. In the steady shearing flow upstream of the cylinder, the polymer molecules near the centreplane are in an unextended, relaxed configuration for all Deborah numbers (since the shear rate along the centreplane is zero); and the velocity profiles near the *upstream* stagnation point at $\zeta = -1$ superpose when scaled with the average velocity $\langle v_z\rangle$ and the cylinder radius R. However, as De is increased, the macromolecules moving very close to the cylinder experience progressively stronger deformation rates which lead to the development of large molecular extensions and high elongational stresses. This deformation is 'remembered' by the fluid, and the configuration of the molecules as they enter the downstream stagnation flow changes with increasing De. The LDV measurements show that very close to the downstream stagnation point ($\zeta \leqslant 1.5$) the velocity profiles superpose, but that as the extension rate and Deborah number increases the velocity of the fluid moving away from the cylinder recovers more slowly to its ultimate value of $v_z/\langle v_z\rangle = 1.5$. These velocity measurements together with other similar LDV profiles measured away from the centreplane (not shown here) indicate clearly that the cylinder wake is extended *downstream* with increasing De, equivalent to a *downstream* shift of the streamlines around the cylinder.

PHILOSOPHICAL TRANSACTIONS OF THE ROYAL SOCIETY A MATHEMATICAL, PHYSICAL & ENGINEERING SCIENCES

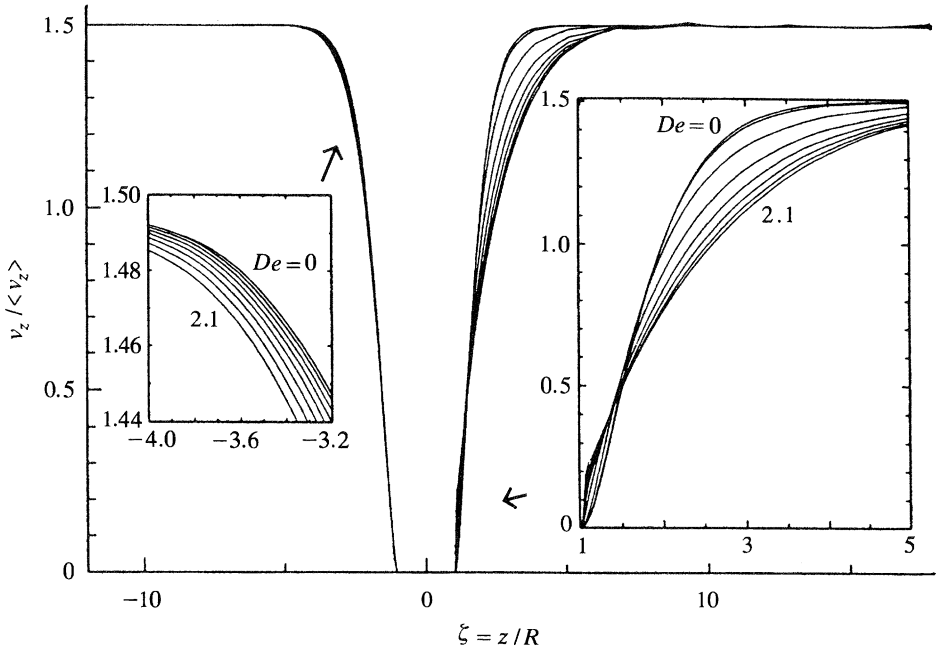

Figure 7. Numerical solutions of the normalized axial velocity profiles $v_z/\langle v_z \rangle$ along the centreline of the channel for Deborah numbers of $De_1 = 0$, 0.3, 0.6, 0.9, 1.2, 1.5, 1.8 and 2.1. Chilcott–Rallison model, $c = 0.6946$, $L = 12$.

Numerical calculations of the variation in the normalized centreplane velocity profile with increasing Deborah number are presented in figure 7 for the Chilcott–Rallison model with $L = 12$. The numerical calculations provide an excellent representation of the changes in the velocity field documented with the LDV system. Upstream of the cylinder the centreline velocity profiles appear to superpose with increasing De, but closer examination of the numerical results shown in the inset indicates a very small upstream shift in the velocity of less than 1 %, which is within the limits of accuracy associated with the LDV system. Downstream of the cylinder, however, the finite element simulations show a more complex behaviour. Very close to the cylinder ($\zeta < 1.5$) the profiles show a small steepening of the velocity gradients with increasing De, followed by a much larger *downstream* shift in the velocity for $\zeta \geqslant 1.5$, in qualitative agreement with the experimental measurements shown in figure 6*b*.

Despite this close similarity between the experimental measurements and calculations, it is important to note the current limitations of such finite element simulations. The results in figure 7 are calculated by progressively incrementing the visoelastic parameter, $De_1 \equiv \lambda_1 \langle v_z \rangle / R$, since this is the dimensionless group that naturally arises during non-dimensionalization of the governing equations (cf. Bird *et al.* 1987*a*). This 'zero-shear-rate Deborah number' is related to our shear-rate-dependent Deborah number De through equation (4), and the numerical results in figure 7 correspond to a maximum value of $De_1 = 2.70$, or $De = 0.80$. Any further increases in De_1 lead to loss of numerical convergence unless a finer finite element mesh is used, as discussed by Lunsmann *et al.* (1993).

Numerical solutions of the velocity and stress fields of the Chilcott–Rallison model at $De_1 = 2.70$ are shown in figures 8 and 9 respectively for a finite-element mesh

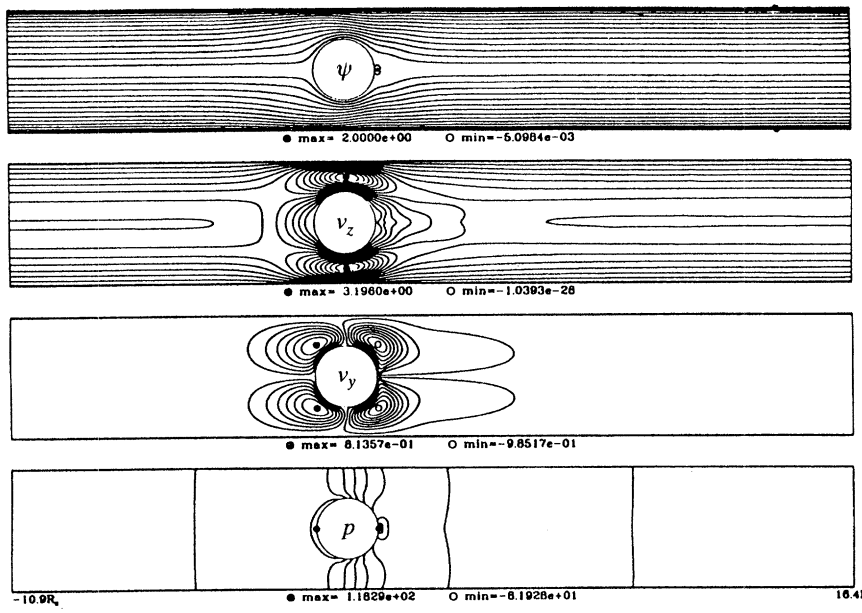

Figure 8. Contours of the dimensionless streamfunction (ψ), streamwise velocity (v_z), transverse velocity (v_y) and pressure fields (p) at $De = 0.69$ ($De_1 = 2.70$), $Re = 0$.

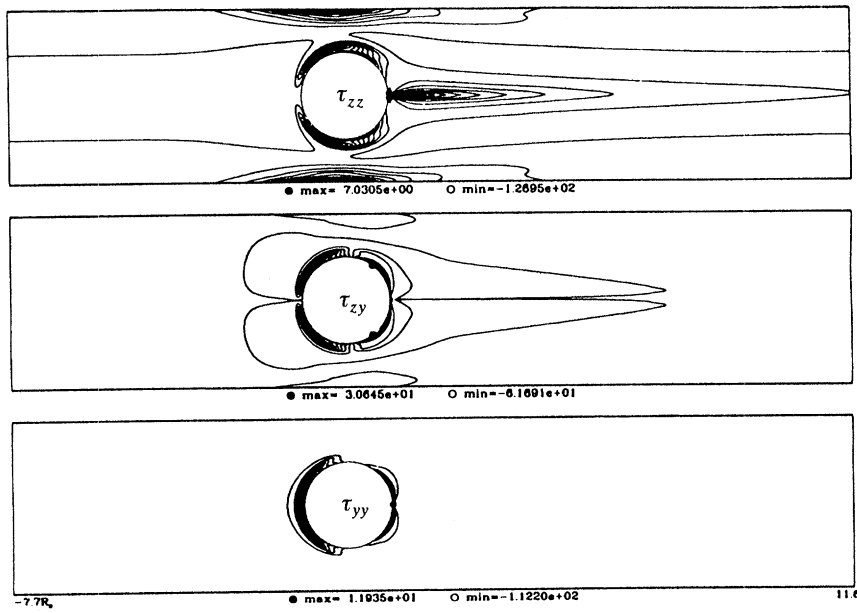

Figure 9. Contours of the dimensionless stress components τ_{zz}, τ_{yy}, τ_{zy} at $De = 0.69$, ($De_1 = 2.70$).

containing 34 908 degrees of freedom (designated mesh M3 in the work of Lunsmann *et al.*). The direction of flow in each figure is from left to right and equally spaced contours are plotted between the minimum and maximum values of each variable across the full computational domain which extends from $-12 \leqslant \zeta \leqslant 18$. The normalized velocity fields and the streamfunction ψ shown in figure 8 indicate the loss of symmetry near the fore and aft stagnation point and the downstream shift in

the streamlines. The steep velocity gradients observed in figure 8 result in the development of large elastic stresses in the flow that are shown in figure 9. In particular, large negative (or tensile) axial stresses τ_{zz} develop in two separate regions of the flow: within the strong shearing flow in the narrow gap between the cylinder and the channel walls, and in the strong extensional flow along the centreplane in the wake of the cylinder. The close spacing of the contours for all three stress components shown in figure 9 indicates the formation of very steep stress boundary layers near the cylinder. The slender sheet of highly elongated molecules along the channel centreplane gives rise to large tensile stresses due to the pronounced extensional-thickening in the planar elongational viscosity predicted by the Chilcott–Rallison model for $L = 12$. The failure to resolve the evolution of this structure is believed to cause the loss of numerical solution beyond a critical Deborah number (Lunsmann *et al.* 1993). The computations can be extended to slightly higher De_1 by refining the mesh still further; however, the calculations become prohibitively expensive and a boundary layer analysis such as that developed by Harlen (1990) for the flow around a sphere in a channel may be more appropriate. Alternatively, Lunsmann *et al.* show that by reducing the extensibility of the molecules to $L = 5$, and thereby reducing the degree of extensional-thickening in the cylinder wake, the computations can be continued with a fixed finite element grid without an apparent upper limit in De_1.

Substituting the maximum value of the zero-shear-rate Deborah number for which finite element solutions were attained into equation (4) corresponds to a shear-rate-dependent Deborah number of only $De = 0.80$. It has not been possible to continue even qualitative comparisons of the steady, two-dimensional LDV measurements beyond this point, even though the experimental data show that viscoelastic flow past the cylinder remains two-dimensional up to a Deborah number of $De \approx 1.3$, which corresponds to $De_1 \approx 3.8$.

4. The elastic wake instability, $De > 1$

LDV measurements have been used to document the spatial and temporal characteristics of a purely elastic flow instability that develops in the downstream wake of the cylinder beyond a critical Deborah number. We first present detailed results for the flow geometry with a cylinder to channel ratio of $\beta = 0.5$ and then examine the variations in the structure of the instability that result from decreasing the cylinder radius and thus reducing the ratio β.

(a) *The onset of steady, three-dimensional flow,* $\beta = 0.50$

Further increases in the Deborah number beyond $De = 0.69$ result in progressively larger downstream shifts in the velocity profiles until the onset of a flow instability occurs at $De = 1.30$. This instability results in a transition from a steady, two-dimensional planar extensional flow in the wake of the cylinder to a steady, but three-dimensional cellular structure which extends along the length of the cylinder. A series of axial velocity profiles in the cylinder wake is presented in figure 10 as the flow rate through the channel is slowly increased. These profiles are measured in the 'neutral' x-direction along the channel symmetry plane very close to the cylinder at $(\nu, \zeta) = (0, 1.5)$, where the velocity is approximately 26 % of its value far downstream; see figure 6. At low flow rates, the LDV velocity measurements in the wake of the cylinder are flat across the central section of the channel, as expected for a steady, planar stagnation flow. However, as De is increased, spatially periodic oscillations

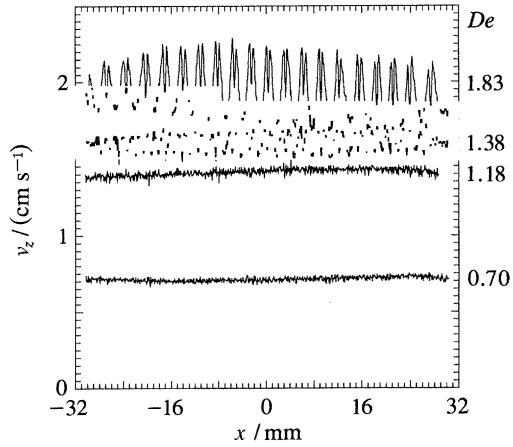

Figure 10. Profiles of the axial velocity $v_z(x)$ across the width of the channel at $(r, \zeta) = (0, 1.5)$ as the Deborah number is increased from $De = 0.70$ to $De = 1.83$.

appear in the velocity profiles; the measurements presented in figure 10 at $De = 1.38$ and 1.83 show the large spatial fluctuations in the axial velocity that extend in the neutral x-direction along the length of the cylinder.

It is important to note here how these LDV data are collected and how they differ from the data presented in earlier figures. To generate these profiles, the measuring volume is positioned at a point x_1 and the computer program controlling the stepper motors then translates the optical table at a fixed velocity, $u_x = 1.00$ mm s^{-1}, to a new point x_2. The instantaneous Doppler frequency measured in the flow is followed in real time by a phase-locked loop in the frequency trackers and after A/D conversion is stored on computer as a file of 1024 evenly spaced data points. The time-dependent signal response is then converted to a spatial velocity profile by a simple mapping as $v_z(x) = v_z(x_1 + u_x t)$. Since the six LDV beams are not mutually orthogonal and intersect the flow cell at an oblique angle it is not possible to follow the velocity profiles directly to the end walls (located at $x = \pm 38.1$ mm); however, the measurements presented in figure 10 and subsequent figures contain velocity measurements across the central 80% of the channel from -30.5 mm $\leqslant x \leqslant +30.5$ mm. In conventional LDV operation, the accuracy of velocity measurements is improved by holding the measuring volume at a fixed point and averaging a large number of discrete Doppler bursts. When the probe volume is translated through space, however, the accuracy is limited by the instantaneous local data rate, which is typically only 50 Doppler bursts per second for slow polymer flows. The rapid small-amplitude fluctuations in the steady planar velocity profile at $De = 0.70$ indicate the maximum level of accuracy (approximately $\pm 3\%$) that can be achieved with the system in this 'instant-acquisition mode'.

The critical Deborah number for the onset of the wake instability was determined by performing a series of velocity scans along the cylinder length as the flow rate was gradually increased. The minimum and maximum amplitudes of the axial velocity measured at a constant axial position of $\zeta = 1.50$ and averaged over the length of the cylinder are shown in figure 11 as a function of De. At low flow rates the axial velocity is constant across the cylinder and increases approximately linearly with De, as shown by the hollow symbols in figure 11. This is in agreement with the results previously presented in figure 6 which show that the normalized velocity at $\zeta = 1.50$

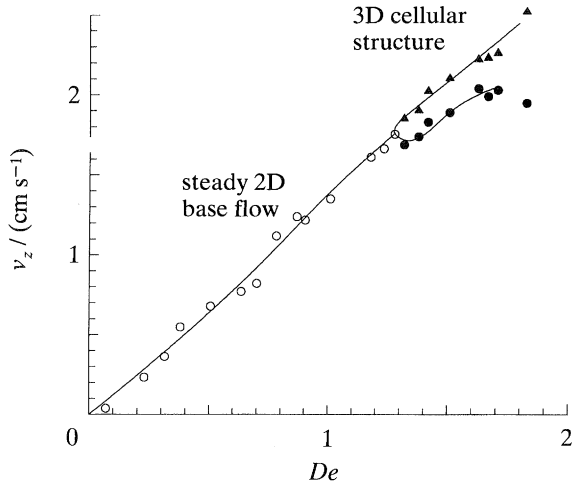

Figure 11. Magnitude of the axial velocity v_z measured in the wake of the cylinder as a function of the Deborah number; hollow symbols (○) indicate the average value of the flat velocity profile in two-dimensional planar stagnation flow; solid symbols indicate the maximum (▲) and minimum (●) values of the velocity fluctuations measured in the cellular wake structure. $(\xi, \nu, \zeta) = 0, 0, 1.5)$.

is almost independent of De. However, at a critical value $De_c = 1.30 \pm 0.01$, spatially periodic oscillations appear in the velocity profiles near the cylinder. The maximum and minimum values of the axial velocity are shown in figure 11 by the solid symbols, and the amplitudes of the fluctuations increase as the Deborah number is increased.

The fluctuations in the axial velocity profiles shown in figure 10 indicate the spatial wavelength of the disturbance, which is quantitatively determined by Fourier analysis of the profile $v_z(x)$. A sample velocity profile measured in the cylinder wake at $\zeta = 1.75$ is shown in figure 12*a*. A fast Fourier transform (FFT) of this signal results in a series of points that are equally spaced in wavenumber or 'spatial frequency' f_x (mm^{-1}). Inversion of these wavenumber values leads to a power spectrum describing the spectral contributions of oscillations with a spatial wavelength of λ_x (mm). The maximum wavenumber is determined by the Nyquist sampling theorem to be $f_{x,\max} = 8.39$ mm^{-1} and the 'bin size' or resolution of the spectrum is determined from the magnitude of the domain as $\delta f_x = \pm 0.016$ mm^{-1}. The characteristic wavelength of the velocity fluctuations determined from the FFT spectrum presented in figure 12*b* is $\lambda_x = 3.03 \pm 0.15$ mm. The wavelength of the disturbances is therefore almost equal to the radius of the cylinder; $\lambda_x = (0.95 \pm 0.05) R$.

The LDV system has also been used to investigate the temporal stability of the flow in the cylinder wake. A sample velocity time-series $v_z(t)$ at a fixed spatial position $(\xi, \nu, \zeta) = (0, 0, 1.75)$ is presented in figure 13 for the same flow conditions as in figure 12. The flow in the cylinder wake consists of oscillations that extend spatially across the length of the cylinder; however, the velocity measured at any single point remains steady in time, and the Fourier spectrum reveals no dominant frequencies of oscillations. Similar results were obtained at points throughout the wake and it is concluded that the elastic instability in the cylinder wake results in the formation of a steady, but three-dimensional flow field.

The video-imaging system described in §2 was used to show unequivocally that these spatial fluctuations in the velocity profiles are associated with the development of an evenly-spaced 'cellular structure' in the cylinder wake. A narrow longitudinal

Figure 12

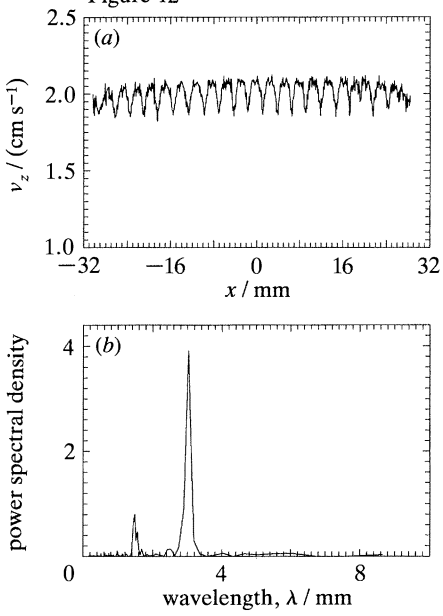

Figure 13

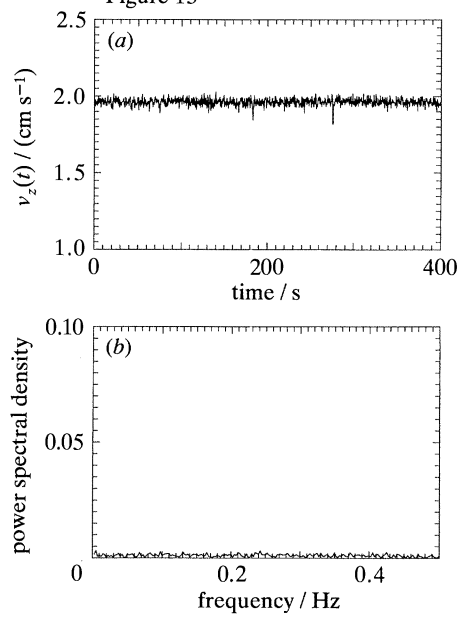

Figure 12. (*a*) Spatial fluctuations in the axial velocity $v_z(x)$ measured in the downstream wake of the cylinder at $\zeta = 1.75$ and flow conditions of $De = 1.38$ and $Re = 0.017$; $(\nu, \zeta) = (0, 1.75)$. (*b*) The FFT spectrum determines the spatial wavelength of the fluctuations as $\lambda_x = 3.03$ mm ± 0.15 mm $= 0.95R$.

Figure 13. (*a*) Time-series of the axial velocity $v_z(t)$ in the cylinder wake at the same position and flow conditions as figure 12. (*b*) The Fourier spectrum reveals no dominant frequencies of osillation.

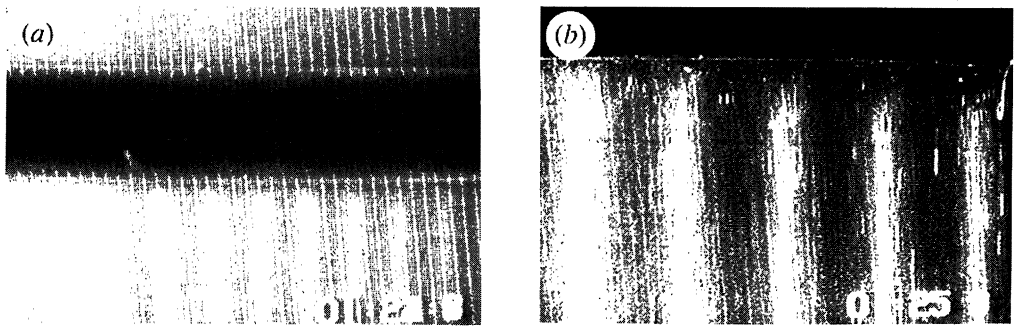

Figure 14. The elastic wake instability at $De = 2.48$, $Re = 0.028$. (*a*) Video-imaging of the flow shows the formation of a cellular structure in the downstream wake that extends along the length of the cylinder; (*b*) higher magnification image close to the downstream stagnation point shows that the velocity in the cylinder wake is three-dimensional with a v_x component parallel to the cylinder axis.

section of the flow at $\nu = 0$ is illuminated with a planar sheet of laser light, and the video camera is aligned with the y-axis to visualize the flow along the length of the cylinder (cf. Cochrane *et al.* 1981). Representative still frames from the videotape are presented in figure 14. In each image the flow is from the top to bottom and the cylinder appears horizontally on the page. The low magnification image presented in

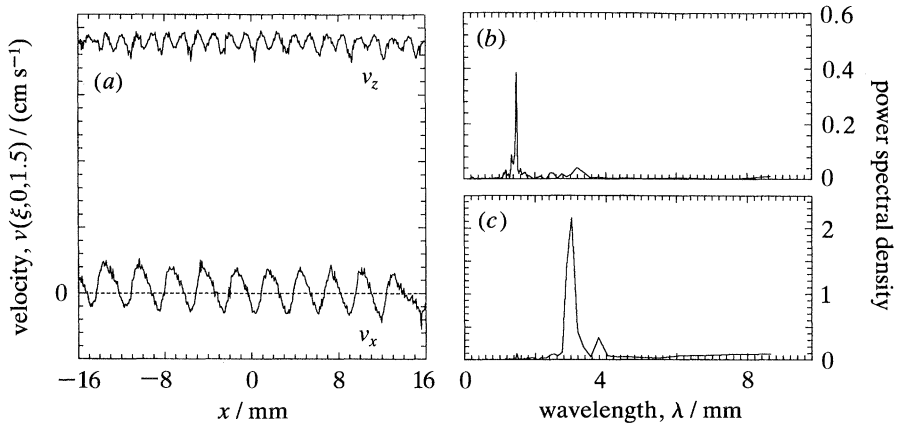

Figure 15. (*a*) Fluctuations in both velocity components $v_z(x)$ and $v_x(x)$ across the width of the channel at $(\nu, \zeta) = (0, 1.5)$ and flow conditions of $De = 1.77$ and $Re = 0.012$; (*b*) the wavelength of oscillations in the axial velocity is determined from the FFT spectrum as $\lambda_x = 1.50 \pm 0.04$ mm; (*c*) the wavelength of oscillations in the x-component velocity is $\lambda_x = 3.03 \pm 0.15$ mm.

figure 4*a* demonstrates the presence of a periodically alternating banded structure in the cylinder wake. Combined LDV measurements and direct visual observation indicate that the bright areas correspond to the regions of higher axial velocity that are observed in velocity scans along the length of the cylinder. Figure 14*a* also clearly shows that the cellular structure extends across the length of the cylinder but is confined to the *downstream* wake; the flow upstream of the cylinder appears spatially uniform, and LDV measurements confirm that the velocity profiles here remain two-dimensional with no spatial fluctuations.

Subsequent flow visualization experiments at higher magnifications show that the velocity field in the cylinder wake is truly three-dimensional, and that particles very close to the cylinder move along the x-axis in both directions as they flow into the faster-moving, brighter regions of the wake. This effect is clearly observed on the videotape but is more difficult to capture in still images. Figure 14*b* shows the velocity field in the cylinder wake at $De = 2.48$; the particle streak in the upper right section shows that there is an x-component of velocity very close to the cylinder.

This complex three-dimensional flow field in the cylinder wake has been carefully explored using the three-colour LDV system. Figure 15*a* shows profiles of the v_x and v_z components of velocity measured on the channel centreline very close to the cylinder at $\zeta = 1.40$ and flow conditions of $De = 1.77$ and $Re = 0.012$. At these conditions the flow around the cylinder remains symmetric about the channel centreplane $\nu = 0$, and no y-component of velocity is measured with the LDV system. The v_x velocity along the cylinder axis oscillates about zero with a spatial wavelength of $0.95R \pm 0.05R$, as fluid flows in both directions along the cylinder from the slower moving regions into each faster moving cell. LDV measurements also show periodic fluctuations in the axial velocity v_z component very close to the cylinder; however, the wavelength of these oscillations is determined from the FFT in figure 15*b* to be $\lambda_x = 0.47R \pm 0.02R$. These measurements show that the axial velocity oscillates with a frequency of twice that observed in the v_x component, and close examination of the velocity profiles shown in figure 15*a* reveals that v_z displays a minimum value at each position where the magnitude $|v_x|$ reaches a maximum.

Similar measurements further from the cylinder at $\zeta = 2.0$ are shown in figure 16.

PHILOSOPHICAL TRANSACTIONS OF THE ROYAL SOCIETY A MATHEMATICAL, PHYSICAL & ENGINEERING SCIENCES

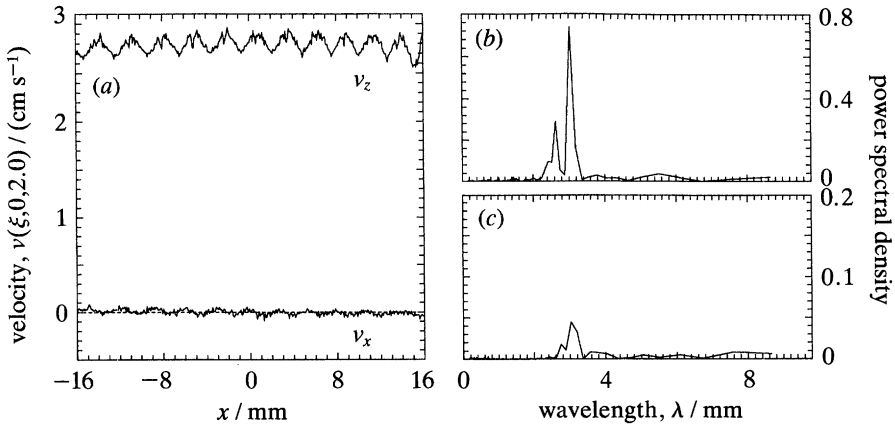

Figure 16. (*a*) Fluctuations in both velocity components $v_z(x)$ and $v_x(x)$ across the width of the channel at $(\nu, \zeta) = (0, 2.0)$ and same flow conditions as figure 15. The wavelength of oscillations in both velocity components is determined from the FFT spectra presented in (*b*) and (*c*) as $\lambda_x = 3.03 \pm 0.15$ mm.

Figure 17

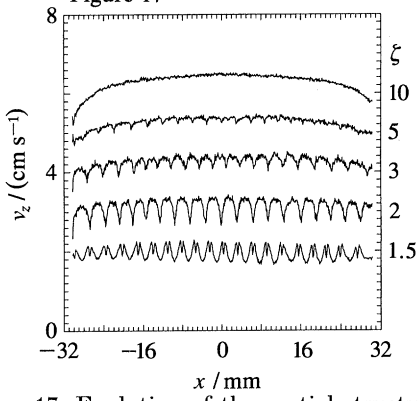

Figure 18

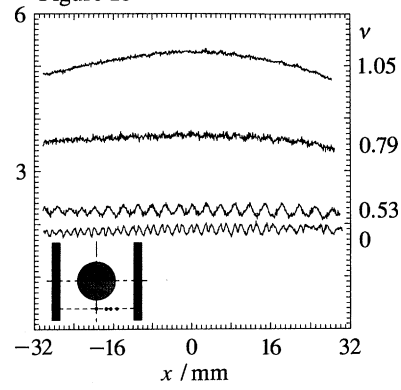

Figure 17. Evolution of the spatial structure observed in the centreline axial velocity $v_z(\xi, 0, \zeta)$ within the downstream wake of the cylinder at $De = 1.83$ and $Re = 0.0158$.

Figure 18. Measurements of the axial velocity profiles along the length of the cylinder at different transverse positions of $y/R = 0$, 0.53, 0.79 and 1.05 show that the three-dimensional cellular structure is confined to a narrow region of the cylinder wake near the channel centreline.

The v_x component of velocity still shows periodic fluctuations about zero; however, the amplitude of oscillations is greatly reduced and the FFT spectrum shows the presence of only a weak peak at $\lambda_x = 0.95R$. The axial velocity v_z at $\zeta = 2.0$ also contains periodic oscillations, though the dominant wavelength of these oscillations shown in figure 16*b* has doubled from those measured at $\zeta = 1.5$ (cf. figure 15*b*) to $\lambda_x = 0.95R$.

The progressive evolution of this cellular structure in the downstream wake of the cylinder is shown in figure 17. Near the stagnation point, at $\zeta = 1.5$, there is motion along the length of the cylinder, and the complex three-dimensional flow results in the rapidly modulated oscillations with wavelengths of $\lambda_x \approx 0.5R$ and $\lambda_x \approx 0.95R$ as discussed above. Further away from the cylinder, at $\zeta = 2.0$ and $\zeta = 3.0$, the oscillations in the v_x component decay, and the fully developed cellular structure is aligned in the streamwise direction with axial velocity fluctuations of period equal to

PHILOSOPHICAL TRANSACTIONS OF THE ROYAL SOCIETY A MATHEMATICAL, PHYSICAL & ENGINEERING SCIENCES

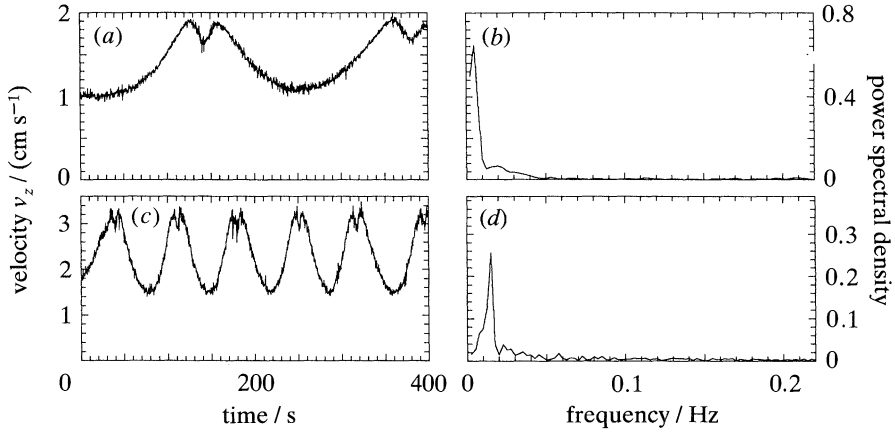

Figure 19. Onset of time-dependent flow in the cylinder wake. (*a*) Experimental time series of axial velocity $v_z(t)$ measured at $(\xi, \nu, \zeta) = (0, 0, 1.4)$, $De = 1.88$ and $Re = 0.0157$; (*b*) FFT spectrum shows very low frequency of oscillation corresponding to a wave speed of $U_x \approx 0.013$ mm s^{-1}; (*c*) velocity time series $v_z(t)$ measured at $(\xi, \nu, \zeta) = (0, 0, 1.5)$, $De = 3.31$ and $Re = 0.0387$; (*d*) FFT spectrum shows an increased frequency of oscillation and a wave speed of $U_x \approx 0.043$ mm s^{-1}.

the cylinder radius. The cells slowly decay at large distances from the cylinder as the fluid in the wake approaches the channel centreline velocity. At a distance of 10 cylinder radii downstream the axial velocity has almost recovered the uniform rectangular channel profile documented in figure 3.

Similar LDV measurements coupled with direct flow visualization show that the three-dimensional wake structure is confined to the narrow region of predominantly extensional flow near the centreplane of the channel. Scans of the velocity at a fixed axial position of $\zeta = 1.50$ and different points in the transverse y-direction are shown in figure 18. On the channel centreplane ($\nu = 0$) the axial velocity has the rapid fluctuations of wavelength $\lambda_x \approx 0.5R$ documented above. The periodic bright and dark cellular structure can still be observed in flow visualization experiments if the plane of laser light is slightly offset from the centreline and the velocity component $v_z(x)$ at $\nu = 0.53$ still shows oscillations, with a period equal to the cylinder radius. However, at greater distances from the centreplane the flow between the cylinder and the channel walls is primarily a steady shearing flow with only a weak elongational component, and LDV measurements of the axial velocity remain almost two-dimensional across the channel for all values of De.

(*b*) *Time-dependent flow in the cylinder wake*, $\beta = 0.5$

As the flow rate past the cylinder is increased further a second flow transition is observed, and LDV measurements for $De \geqslant 1.85$ show that the flow in the wake becomes time-dependent. Representative time-series of the axial velocity in the cylinder wake at $(\xi, \nu, \zeta) = (0, 0, 1.4)$ are shown in figure 19. The velocity $v_z(t)$ shows a nonlinear time-periodic response on a time-scale of hundreds of seconds. Video-imaging of the flow reveals that the cells observed in the wake slowly travel outwards from the midpoint of the cylinder $(\xi, \nu) = (0, 0)$ towards the side-walls of the channel. The time-dependent response in the velocity measured at a fixed point in space thus corresponds to the slow translation of this regular cellular structure through the measuring volume, and the nonlinear form of the oscillations arises from the complex spatial structure of the axial velocity profile at $\zeta = 1.4$ (cf. figure 17). The wavespeed

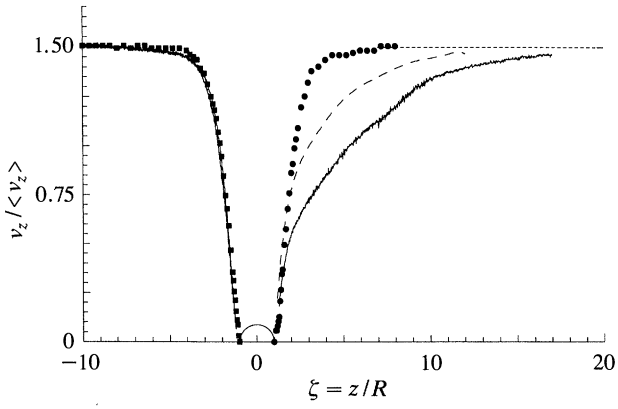

Figure 20. Centreline axial velocity profiles in the three-dimensional wake at high Deborah numbers show a pronounced shift downstream but increase monotonically to the free stream value with no 'negative wake' or aperiodic fluctuations. (●) Slow flow, $De = 0.073$, $Re = 0.0055$. (– – –) $De = 1.71$, $Re = 0.014$. (——) $De = 3.09$, $Re = 0.028$. $(\xi, \nu) = (0, 0)$.

for this travelling structure is calculated from the spatial wavelength λ_x of the cells and the temporal frequency of the velocity time-series determined by the FFT spectra shown in figure 19*b*, *d*. As the Deborah number is raised from $De = 1.88$ to $De = 3.31$, the frequency of oscillations increases and the wavespeed increases from $U_x = 0.013$ mm s^{-1} to $U_x = 0.043$ mm s^{-1}.

Time-dependent velocity oscillations in the wake of a cylinder are encountered in high Reynolds number flows of newtonian fluids and very dilute polymer solutions due to the formation of a von Kármán 'vortex street'; however, the maximum Reynolds number attained in the experiments with this Boger fluid is only $Re \approx 0.04$. The onset of time-dependence in the cylinder wake results solely from translation of the cellular structure along the length of the cylinder and not from a periodic 'vortex shedding' phenomenon in the stream-wise direction. Profiles of the centreline axial velocity in the stagnation flows upstream and downstream of the cylinder are shown in figure 20. These velocity measurements are made with the frequency trackers by using the instantaneous acquisition algorithm described above and translating the table in the z-direction at a constant velocity of $u_z = 1.50$ mm s^{-1}. The total data acquisition time for each profile $v_z(z)$ is only 30 s which is much smaller than the period of oscillation documented in figure 19 for translation of the cellular structure by one wavelength λ_x along the cylinder axis. Thus, each profile represents the evolution of the wake axial velocity profile within one cell as the fluid accelerates back up to the free stream value. The velocity profiles upstream of the cylinder superpose when normalized with the average velocity $\langle v_z \rangle$, and elasticity does not affect the upstream stagnation flow even at Deborah numbers of $De > 3$. However, in the wake downstream of the cylinder, elastic effects result in a progressive downstream shift in the position of the streamlines around the cylinder. The LDV measurements for newtonian flow at $De = 0.07$ are also shown in figure 20 to emphasize the magnitude of this downstream displacement; at a fixed point $\zeta = 5$, the normalized axial velocity at $De = 3.08$ has been reduced by approximately 33% from its value at $De = 0.07$, and the flow does not recover a fully developed parabolic profile for distances of over $15R$ downstream of the cylinder.

(c) *The effect of the cylinder-channel ratio, β*

The wavelength of the cellular wake structure for a cylinder-channel ratio of $\beta = 0.5$ was determined from the measurements in §4*a* to correlate closely with the radius R of the cylinder. However, this observation is ambiguous since the narrow gap $(H-R)$ between the cylinder and the constraining channel wall is identical to the cylinder radius for $\beta = 0.5$. To investigate the scaling of the cellular structure with the flow geometry, additional experiments were performed with a series of cylinders of smaller radii, which were mounted in the same channel of constant half-width, $H = 6.33$ mm. In this manner the cylinder-to-channel ratio was successively reduced to $\beta = 0.337$, $\beta = 0.257$, and $\beta = 0.170$.

In addition to the Deborah number defined in (1), which is based on the residence time for polymer molecules near the cylinder, a *Weissenberg number* can be defined in terms of the characteristic shear rate $\dot{\gamma} = \langle v_z \rangle/(H-R)$ measured in the gap between the cylinder and the channel wall as

$$We \equiv \lambda(\dot{\gamma})\langle v_z \rangle/(H-R). \tag{5}$$

The relative magnitude of these two dimensionless groups can be varied by changing the geometric parameters R and H. Substitution of the cylinder–channel ratio $\beta = R/H$ into (5) shows that the two parameters are interrelated by $We \equiv \beta De/(1-\beta)$. Hence, for a cylinder–channel ratio of $\beta = 0.5$, the Weissenberg number is equal in magnitude to the Deborah number; however for a smaller ratio of $\beta = 0.25$ the larger gap between the cylinder and the channel wall results in lower shear rates, and the Weissenberg number is given by $We = 0.33De$.

LDV measurements in each geometry show that both the cylinder radius and the channel half-width are important in governing the evolution of the velocity field around the cylinder; profiles of the normalized velocity do not superpose, even at very low De, when the axial position is scaled with either R or H. This can be explained by considering the flow in a cylindrical coordinate system (r, θ, x) aligned along the symmetry axis of the cylinder. If we consider finding a solution to the stagnation flow by the method of images (cf. Bairstow *et al.* 1923) then we would expect the local fluid velocities will be perturbed by the cylinder out to a characteristic radial position of $r \sim H$ which is determined by the separation of the rigid channel walls. Along the channel centreline ($\theta = 0$ and $\theta = \pi$) this equates to a streamwise distance of $z \sim H$ that is independent of cylinder radius. The fluid in the planar stagnation flow has to decelerate as it approaches the stagnation points S_1 and S_2; however, since these stagnation points are located at radial positions of $r \sim R$ the characteristic velocity gradients in the stagnation flow are $\langle v_z \rangle/(H-R)$. Smaller cylinders therefore result in a more gradual change in the v_z velocity. The competing influences of the confining channel walls and the size of the cylinder in the channel can both be taken into account by defining a modified dimensionless coordinate $\zeta^* = (z-R)/H$ which is zero at the stagnation points S_1 and S_2 for all β. Profiles of the normalized centreplane velocity $v_z(\zeta^*)/\langle v_z \rangle$ for each cylinder to channel ratio are shown in figure 21 at a constant value $De = 0.14$. The velocity profiles collapse to a single master curve and superpose in the regions very close to the stagnation points $(z \sim R)$ and also at larger distances into the channel $(z \sim H)$ where the constraining effects of the walls become important.

Further experiments at higher De show that the formation of a three-dimensional cellular structure is observed for each value of β studied, and that the dynamics of

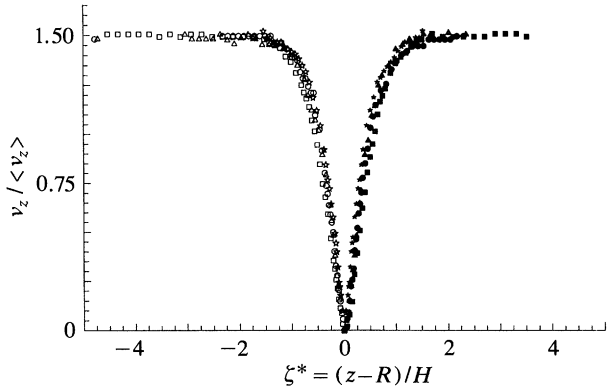

Figure 21. Effect of the cylinder-channel ratio β on the centreplane axial velocity profiles in the stagnation flow near the cylinder at a fixed Deborah number of $De = 0.14$. Hollow symbols denote the upstream flow and solid symbols denote the downstream flow for cylinder-to-channel ratios of: (★) $\beta = 0.170$, (●) $\beta = 0.257$, (▲) $\beta = 0.337$ and (■) $\beta = 0.503$. $(\xi, \nu, \zeta) = (0, 0, \zeta)$.

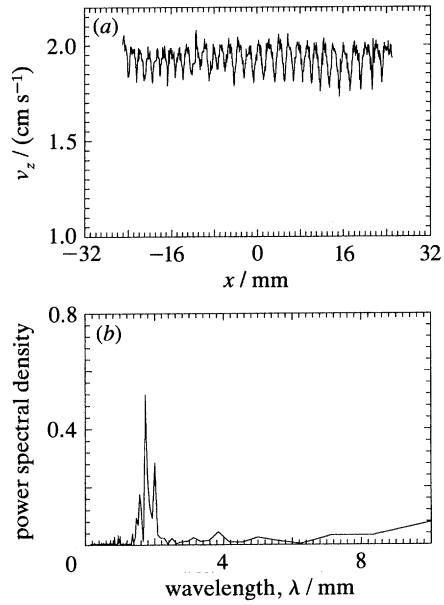

Figure 22. (*a*) Spatial fluctuations in the axial velocity $v_z(x)$ measured in the downstream wake of the smallest cylinder ($\beta = 0.170$) at $De = 3.18$ and $Re = 0.0039$. (*b*) The FFT spectrum determines the dominant spatial wavelength of the fluctuations as $\lambda_x \approx 1.72 \pm 0.14$ mm.

this elastic wake instability are dependent on both the Deborah number and the Weissenberg number. The centreline axial velocity profile along the length of a cylinder with radius $R = 1.08$ mm ($\beta = 0.17$) is shown in figure 22*a* for flow conditions of $De = 3.18$ and $We = 0.75$. The velocity in the wake shows periodic fluctuations similar to those presented in §4*a*; however, the oscillations have a reduced wavelength of $\lambda_x = 1.72$ mm, equivalent to 1.6 times the new cylinder radius. The power spectrum shown in figure 22*b* indicates that the wavelength selection of the velocity fluctuations is not as clearly defined in this geometry and secondary peaks are observed at $\lambda_x = 1.58$ mm and $\lambda_x = 2.03$ mm. The spatial

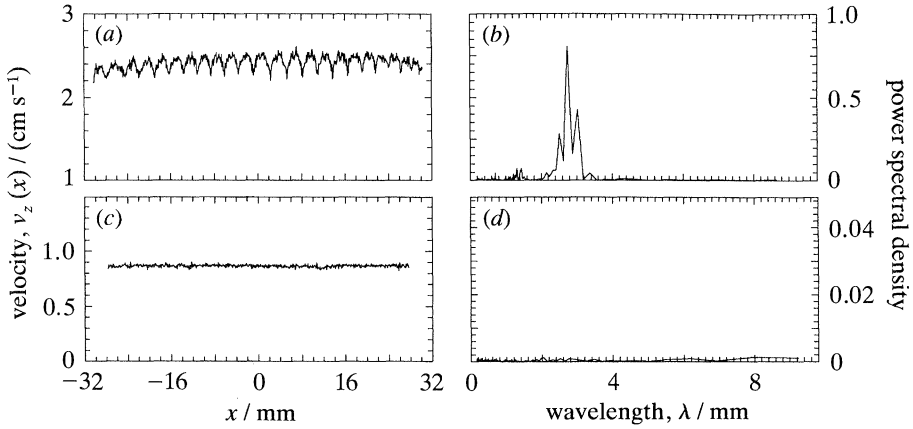

Figure 23. Comparison of the centreline axial velocity component $v_z(x)$ at $De = 1.38$ for two different cylinder–channel ratios. (*a*) Velocity fluctuations at $\zeta = 2.0$ for larger cylinder–channel ratio of $\beta = 0.503$. (*b*) The dominant wavelength of oscillations is determined from an FFT as $\lambda_x = 3.03$ mm. (*c*) Planar velocity profile at $\zeta = 2.0$ for smaller cylinder–channel ratio of $\beta = 0.257$. (*d*) FFT reveals no cellular structure in the cylinder wake.

Table 1. *Spatial wavelength of the three-dimensional viscoelastic wake structure downstream of circular cylinders*

cylinder-channel ratio, β	radius, R/mm	wavelength, λ_x/mm	λ_x/R
0.503	3.188	3.03 ± 0.15	0.95
0.337	2.135	2.55 ± 0.12	1.19
0.257	1.628	2.30 ± 0.10	1.41
0.170	1.075	1.72 ± 0.20	1.60

wavelength of the three-dimensional wake structure for each geometry is summarized in table 1.

Previous work on viscoelastic transitions in rotational flow has shown that the onset of instabilities depends on both viscoelastic flow parameters De and We. To determine the critical conditions for development of the wake instability in this geometry a large series of experiments were performed which duplicated the stability measurements documented in §4*a* for each value of the ratio β at (i) the same volumetric flow rates or average velocity $\langle v_z \rangle$, (ii) the same Deborah numbers De and (iii) the same Weissenberg numbers We. Two representative results for ratios of $\beta = 0.25$ and $\beta = 0.50$ are presented in figures 23 and 24. Measurements of the axial velocity component $v_z(x)$ at $\zeta = 2.00$ for the two different cylinder to channel ratios at a constant Deborah number $De = 1.38$ are shown in figure 23. The flow past the larger cylinder ($\beta = 0.50$) shows spatially periodic oscillations in the cylinder wake with a cellular wavelength of $\lambda_x = 0.95R$, whereas the flow near the smaller cylinder ($\beta = 0.25$) remains two-dimensional with no velocity fluctuations along the length of the cylinder.

Similar measurements of the axial velocity component $v_z(x)$ for the two different cylinder–channel ratios at the same average upstream velocity $\langle v_z \rangle = 3.71$ cm s^{-1} are shown in figure 24. The volumetric flow rate Q and average velocity are the same for each geometry; however the Deborah number for the geometry with the smaller radius cylinder is approximately twice that for $\beta = 0.50$. The larger gap between the

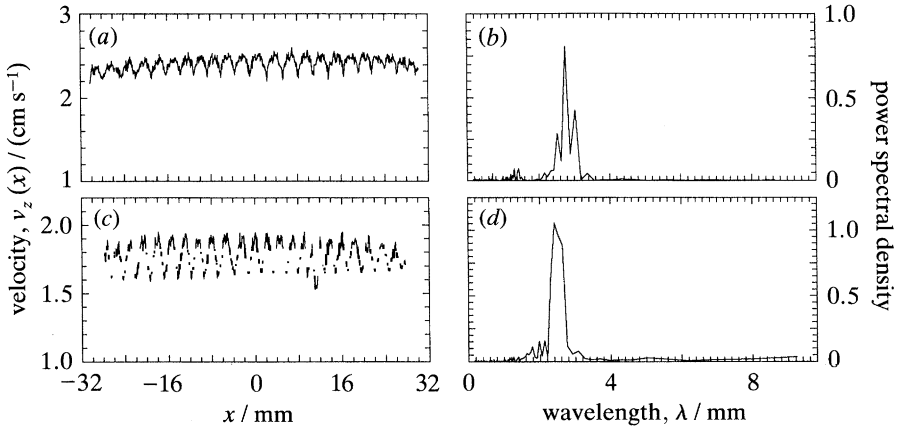

Figure 24. Comparison of the axial velocity component $v_z(x)$ at the same upstream flow conditions $\langle v_z\rangle/H = 5.86\ \text{s}^{-1}$ for two different values of the cylinder–channel ratio β. (*a*) Larger cylinder–channel ratio of $\beta = 0.503$ at flow conditions $De = 1.38$, $We = 1.38$ show velocity fluctuations (*b*) of dominant wavelength $\lambda_x = 3.03$ mm. (*c*) Velocity profiles at $\zeta = 3.0$ for smaller cylinder–channel ratio of $\beta = 0.257$ and $De = 2.57$, $We = 0.94$ show velocity fluctuations (*d*) with reduced wavelength $\lambda_x = 2.40$ mm.

Table 2. *Critical flow conditions for onset of the three-dimensional wake instability in viscoelastic flow past a cylinder*

β	R/cm	$\langle v_z\rangle_c$/(cm s^{-1})	$\dot{\gamma}_c$/s^{-1}	De_c	We_c	Re_c
0.170	0.1075	2.25	20.97	2.35±0.08	0.53±0.02	0.0031
0.257	0.1628	2.64	16.20	1.87±0.13	0.68±0.04	0.0055
0.337	0.2135	3.31	15.48	1.80±0.04	0.95±0.02	0.0090
0.503	0.3188	3.49	10.93	1.30±0.01	1.30±0.01	0.0142

channel wall and the cylinder edge for $\beta = 0.25$ however results in a *smaller* value of the Weissenberg number. Periodic oscillations are observed in both velocity profiles, and the difference in the wavelength of these oscillations is discernible in the FFT spectra presented in figure 24*b*, *d*. If the flow rate through the $\beta = 0.25$ configuration is increased further so that equivalent values of the Weissenberg number are attained in each geometry, the flow past the smaller cylinder remains unstable, though the amplitude of the velocity oscillations increases significantly.

A sequence of experiments for a number of intermediate flow rates between those presented in figures 23 and 24 were performed to determine the critical conditions for the onset of the elastic wake instability in each geometry. These critical conditions, indicated by a subscript c for the four different cylinder–channel ratios studied in this work are summarized in table 2.

The experimental measurements in each geometry have been used to construct an approximate stability diagram for viscoelastic flow past a cylinder in a channel. The results for the four cylinder–channel ratios are shown in figure 25. Stability measurements performed by increasing the volumetric flow rate for a fixed geometric ratio β lie along lines in Weissenberg–Deborah number space with constant slope $We/De = \beta/(1-\beta)$. The abscissa corresponds to the case of a cylinder in an unbounded viscoelastic fluid ($\beta \to 0$). For low flow rates the velocity profiles in the wake of the cylinder are flat, and the flow is steady and two-dimensional. At the critical conditions given in table 2 this base flow becomes unstable, and the velocity

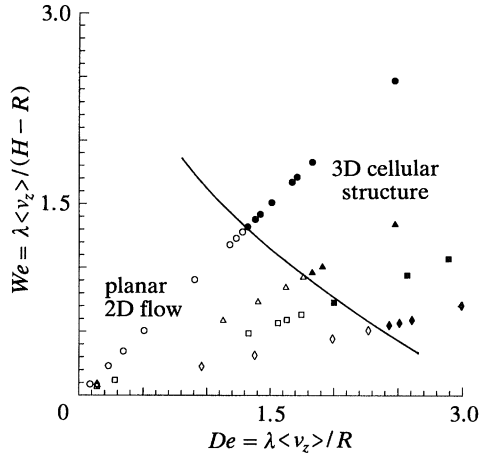

Figure 25. A stability diagram for viscoelastic flow past cirular cylinders of radius R in planar channels of half-height H. The flow in the wake of the cylinder is a steady two-dimensional stagnation flow at low Deborah numbers (hollow symbols) but develops a three-dimensional cellular structure at high De (filled symbols).

profiles in the cylinder wake develop the three-dimensional cellular structure documented above. It can be seen from figure 25 and table 2 that the onset point of the transition varies with the cylinder–channel ratio β; however, measurements indicate that the critical Deborah number De_c increases by only 30% as the cylinder–channel ratio is decreased from $\beta = 0.50$ to $\beta = 0.26$, whereas the critical Weissenberg number is reduced by a factor of 2. These observations suggest that the onset point of the transition and the wavelength of the cellular structure scale more closely with the Deborah number and the cylinder radius; although a weaker modulation on the Weissenberg number and the channel gap is also evident. A more complete evaluation of the We/De parameter space contained in the stability diagram requires a large number of additional experiments for different cylinder-to-channel ratios β.

5. Conclusions

The LDV technique has proved to be an extremely powerful tool for exploring the flow transitions that are observed in viscoelastic flows through complex geometries. The measurements presented in this work are the first experimental observations of a three-dimensional elastic instability that occurs within the planar extensional flow in the wake of a circular cylinder. At a critical Deborah number the steady two-dimensional flow undergoes a bifurcation to a steady, three-dimensional motion consisting of a spatially periodic cellular structure that extends along the length of the cylinder. The LDV measurements coupled with video flow visualization clearly show that this structure corresponds to cells of fluid moving with a local axial velocity that is higher than the average value. To satisfy continuity constraints these regions are supplied with fluid from neighbouring slower moving cells on either side. The flow remains symmetric about the channel centreplane ($y = 0$) and there is no measurable v_y velocity component in this plane (within the resolution of the three-colour LDV system). It is thus possible to define local streamlines for this two-dimensional planar region, and figure 26 shows a sketch representing the fluid streamlines along the central plane of the channel which helps explain the complex

PHILOSOPHICAL TRANSACTIONS OF THE ROYAL SOCIETY A MATHEMATICAL, PHYSICAL & ENGINEERING SCIENCES

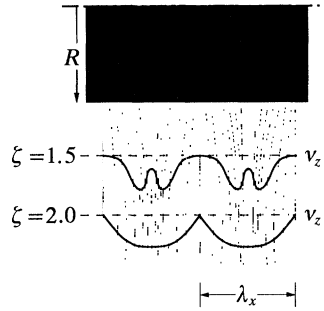

Figure 26. An approximate representation of the streamlines along the channel centre-plane ($y/R = 0$) showing the spatial evolution of the velocity profiles and the development of a cellular structure in the cylinder wake.

oscillations in the velocity field that have been documented in figures 15–17. Near the cylinder at $\zeta = 1.5$ the streamlines are curved and the velocity has significant v_z and v_x components, as fluid alternately converges into the faster moving regions (corresponding to the brighter regions in figure 14*b*) and diverges from the slower moving areas. A profile of the axial velocity at this point shows periodic oscillations with a wavelength $\lambda_x \approx \frac{1}{2}R$. Farther downstream of the cylinder the cells are fully developed and the streamlines are almost parallel to each other. The v_x component of velocity decreases and for $\zeta > 2.0$, the wake consists of a regularly spaced cellular structure with periodic fluctuations in the velocity of wavelength $\lambda_x \approx R$.

The first observations of cellular-type instabilities in duct flows of viscoelastic fluids were made by Giesekus (1972). Photographs of polyisobutylene solutions discharging at high shear rates from channels of rectangular cross-section showed the formation of regularly spaced 'grooves' in the surface of the jet which travelled outwards from the midpoint towards the edges of the channel. Subsequent observations of this transition by Tomita & Takahashi (1978) demonstrated that the spacing of the cells depended on the aspect ratio of the channel, but was essentially a free-surface phenomenon associated with the die-swell at the exit of the duct and independent of the upstream flow configuration.

Very recently Chiba *et al.* (1990) have presented qualitative flow visualization images that reveal the onset of a similar cellular transition in the viscoelastic flow of a dilute, shear-thinning, aqueous polyacrylamide solution through a 10:1 planar contraction. Streak photographs of longitudinal cross-sections through the contraction (i.e. along the neutral axis) reveal that, at a critical flow rate, the planar extensional flow along the contraction centreline becomes unstable and develops a three-dimensional structure. This three-dimensional motion consists of an approximately periodic array of cells which arise from faster and slower moving regions of fluid that are spaced along the neutral axis of the planar contraction. At higher flow rates these 'bundle-like streams' were also observed to travel slowly across the width of the contraction. More recent streak line observations in a 5:1 planar contraction showed that these structures appear to have the form of Görtler vortices with significant streamwise vorticity (Chiba *et al.* 1992). Unfortunately, few quantitative details of the spatial wavelength and critical conditions for the onset of this instability were provided by the authors, but the high flow rates and shear-thinning character of the test fluid resulted in Reynolds numbers of $17 \leqslant Re \leqslant 53$ in the unstable flow régime. It thus seems that inertial effects in the contraction flow

transition are also important, in contrast to our observations of the planar stagnation flow instability.

A previously observed transition that results in anomalous transport properties in the flow of dilute polymer solutions past very small cylinders was discussed in §1. Experimental correlations of the heat transfer and drag coefficients were given by James & Acosta, and have recently been reproduced numerically by Hu & Joseph (1990) and Delvaux & Crochet (1990). The numerical calculations considered high Reynolds number flow past a cylinder for an upper-convected Maxwell (UCM) fluid model, and showed that the asymptotic behaviour of the transport properties observed by James and Acosta corresponded to a change of type in the governing equation set. To interpret their results, Hu and Joesph introduced the concept of a viscoelastic Mach number $M \equiv \langle v_z \rangle / c$, where c is the shear-wave speed for the UCM model, $c \equiv \eta_0 / \rho \lambda_0$ (Joseph & Saut 1986). For $M < 1$ the governing equation set for viscoelastic flow of the UCM model is elliptic and the velocity solutions are smooth everywhere; however, for $M \geqslant 1$, i.e. for velocities greater than the wave speed, the equation set becomes hyperbolic and discontinuities, or shocks, can propagate along the fluid streamlines.

To investigate whether the experimental measurements of the elastic wake instability presented in §4 correspond to a change of type in the flow it is necessary to know the shear-wave speed c for the test fluid. The rheological characterization presented by Quinzani *et al.* has shown that the viscoelastic material functions of the 0.31 % (by mass) PIB/PB/C14 Boger fluid are not accurately described by a single-mode, quasi-linear constitutive equation such as the UCM model, and it not appropriate to use the simple expression above to calculate the wave speed. Recently, Northey *et al.* (1989) have presented a type analysis for a multimode formulation of the UCM model and show that the critical wave speed for propagation of vorticity information is

$$c = \sqrt{\left[\frac{1}{\rho} \sum_{k=1}^{N} \frac{\eta_k}{\lambda_k}\right]}, \tag{6}$$

where η_k and λ_k are the viscosity and time constant of the kth relaxation mode, and ρ is the fluid density.

The shear-wave speed c can be evaluated for the 0.31 % (by mass) PIB Boger fluid by using the set of $\{\eta_k, \lambda_k\}$ determined from linear viscoelastic measurements. However, it is seen from (6) that the presence of a large newtonian solvent viscosity η_s with a time constant $\lambda_s = 0$ results in an infinite wave-speed, and prohibits a change-of-type in the governing equation set. Experiments at very high shear-rates ($\dot{\gamma} > 1000\ \mathrm{s}^{-1}$) in a capillary rheometer show that, in reality, the highly viscous polymeric PB/C14 solvent is not truly newtonian, but very weakly elastic with a relaxation time of $\lambda_s \approx 10^{-4}$ s (McKinley 1991). By combining this estimate for the PB/C14 solvent relaxation time with the four mode spectrum given in Quinzani *et al.*, the speed of shear waves through the Boger fluid is calculated to be $c = 9.61\ \mathrm{m\ s}^{-1}$. Joseph *et al.* (1986) have developed a 'wave-speed meter' to determine experimentally shear-wave speeds for a large number of different liquids, and the value calculated above agrees extremely well with the range of values $8.37 \leqslant c \leqslant 22.40\ \mathrm{m\ s}^{-1}$ measured by Joseph *et al.* for a Boger fluid consisting of 0.25 % (by mass) PIB in polybutene. The calculated value of $c = 9.61\ \mathrm{m\ s}^{-1}$ is far greater than the values of the critical velocity $\langle v_z \rangle_c$ given in table 2, and calculation of the 'viscoelastic Mach number' at the onset of the elastic wake instability reveals it to

be only $M = 3.63 \times 10^{-3}$ for $\beta = 0.50$. Hence, it appears clear that the transition to three-dimensional flow in the wake is not a change-of-type phenomenon and is completely unrelated to the high Re experiments of James & Acosta and the related LDV measurements of Koniuta *et al.* (1980).

The LDV measurements of Bisgaard (1983) for viscoelastic flow past a sphere falling through a cylindrical tube have indicated an elastic wake instability at low Re that results in spatial fluctuations of the velocity in the wake. Measurements of the centreline velocity profile in the tube showed that the velocity behind the trailing stagnation point on the sphere did not decrease monotonically but developed rapid aperiodic fluctuations. In contrast, the LDV measurements presented in figure 20 show that profiles of the velocity in the wake vary smoothly and monotonically in the downstream direction, and the instability in the cylinder wake results in a transition to a steady three-dimensional flow with a well-defined periodic spatial structure. Unfortunately, Bisgaard's data is insufficient to infer the spatial and temporal structure of the flow in the wake of the sphere. However, the presence of velocity fluctuations in the strong shearing flow between the sphere and the tube walls which developed at values of De lower than those required for the formation of aperiodic fluctuations in the wake of the sphere, were also reported. No similar fluctuations were observed in LDV measurements near the cylinders studied in the present work, and the three-dimensional flow is limited to the region of strongly extensional flow in the wake of the cylinder.

The elastic instabilities observed in the wakes of cylinders and spheres appear to be fundamentally different in both their spatial and temporal characteristics. Of course, this is subject to the important caveat that the experiments of Bisgaard were performed with a shear-thinning polymer solution rather than a constant viscosity Boger fluid and for values of the sphere to tube radius ratio in the range $0.06 \leqslant \beta \leqslant 0.18$. It is pointed out by Larson (1992) that both the fluid rheology and relevant dimensionless geometric parameters are extremely important in governing the precise dynamic behaviour associated with the onset of a viscoelastic flow transition. However, it now appears clear from the LDV measurements of Bisgaard plus those presented in this work that both uniaxial and planar extensional flows of viscoelastic fluids near the downstream stagnation points of submerged bodies can become unstable at high Deborah numbers.

The velocity measurements of Sigli & Coutanceau (1977) and Bisgaard (1983) for shear-thinning polymer solutions have both documented the existence of a 'negative wake' in the steady extensional flow behind a sphere. This *velocity overshoot* develops at low Deborah numbers and is not associated with the onset of time-dependent flow. However, the LDV measurements in the cylinder wake for the 0.31% (by mass) PIB Boger fluid show that the velocity monotonically increases from zero to the free stream centreline value $v_z = 1.5\langle v_z \rangle$ at all Deborah numbers (cf. figures 6 and 20). Maalouf & Sigli (1984) used streak photography to show that the velocity profiles measured for a Boger fluid in the wake of a sphere were shifted downstream at high De but remained monotonic; however similar measurements of the velocity profiles for shear-thinning polymer solutions indicated the presence of a velocity overshoot and a 'negative wake' behind the sphere. These earlier observations of no velocity overshoot in Boger fluids are consistent with our measurements in the wake of cylinders for a wide range of ratios β, and it is concluded that a negative wake will only observed in stagnation flows of viscoelastic fluids which exhibit a shear-thinning viscosity $\eta(\dot{\gamma})$.

PHILOSOPHICAL TRANSACTIONS OF THE ROYAL SOCIETY A MATHEMATICAL, PHYSICAL & ENGINEERING SCIENCES

In this work we have only considered one particular viscoelastic fluid, a constant viscosity Boger fluid consisting of polyisobutylene dissolved in polybutene. It is becoming increasingly clear that viscoelastic transitions depend not only on gross rheological characteristics, such as the presence or absence of shear-thinning in the viscosity, but also on the details of the macromolecular structure and the polymer/solvent interactions. The recent work of Chmielewski *et al.* (1990) investigated the elastic dependence of the drag coefficient for spheres falling through Boger fluids consisting of both PIB and PB, and also polyacrylamide (PAA) dissolved in viscous cornsyrup (CS). Measurements showed that the PAA/CS fluid exhibited a monotonic decrease in the drag coefficient below the Stokes value, whereas measurements for the PIB/PB Boger fluid showed a very small initial decrease in the drag coefficient for $De \leqslant 0.3$, followed by a somewhat larger drag *increase* at higher De. Similar drag increases for another PIB/PB fluid formulation have also been presented by Tirtaatmadja *et al.* (1990), and it is possible that the pronounced increase in the drag coefficient observed for $De > 1$ arises from the onset of a similar elastic wake instability in the axisymmetric stagnation flow behind the sphere. Further LDV measurements are currently underway to investigate this possibility.

The dissimilar behaviour of the two Boger fluids indicates that the molecular environments of the PIB and PAA macromolecules in solution are not the same, even though rheological measurements of the viscometric properties (η, Ψ_1) are identical. The stagnation flow in the wake of spheres and cylinders are strong extensional flows, and it seems that the differences in dynamic behaviour must result from different elongational properties of the PIB and PAA chains. The extensive flow visualization results of Boger (1987) also reveal differences in the sequence of viscoelastic flow transitions observed in the strongly extensional flows of PIB/PB and PAA/CS fluids through axisymmetric abrupt contractions. It therefore appears that the stability of complex flows of Boger fluids is a sensitive function of the elongational properties of the polymer molecules in solution. The construction of stability diagrams from LDV measurements or from theoretical analyses can provide a rational interpretation of these differences in terms of the particular ordering of a sequence of nonlinear hydrodynamic transitions. A similar dependence of the critical onset conditions and precise dynamic behaviour is expected in observations of the elastic wake instability (if it exists) for PAA/CS Boger fluids. To explore this variation further, additional LDV measurements are required for a PAA/CS fluid with the same rheological properties as the 0.31 % (by mass) PIB/PB Boger fluid used in the current work.

The Chilcott–Rallison constitutive equation provides a convenient basis on which to perform numerical investigations of this premise, because the extensional rheology can be systematically modified by varying the extensibility parameter L. The variations in the steady two-dimensional velocity around spheres and the evolution of drag coefficient with increasing De and L have already been presented (Lunsmann *et al.* 1993) and work is beginning on numerical studies of the flow stability.

One of the most general conclusions to be drawn from this work is that the base symmetry of the problem appears to be crucial in defining the spatial and temporal structure of viscoelastic flow transitions. In axisymmetric problems, such as Taylor–Couette flow and tubular entry flows, elastic effects lead to the onset of Hopf bifurcations at $De \approx 1$ and the development of flow regimes that are both time dependent and three dimensional. As the Deborah number is increased, subsequent transitions lead to period-doubling, quasi-periodic and finally aperiodic states. By

PHILOSOPHICAL TRANSACTIONS OF THE ROYAL SOCIETY A MATHEMATICAL, PHYSICAL & ENGINEERING SCIENCES

contrast, the few experimental investigations of viscoelastic flow instabilities in planar geometries, (e.g. extrusion from a slit die, planar entry flows and flow past cylinders) indicate that the first flow transition is a bifurcation from a steady two-dimensional flow to a steady, three-dimensional flow that has a periodic, cellular structure in the 'neutral' direction. Only at higher *De* does a second flow transition result in the development of time-dependent flow. This time-dependent motion typically manifests itself as a translation of the periodic structure along the direction of the neutral axis toward the edges of the test geometry.

This work has been sponsored by the Office of Naval Research and the National Science Foundation. We thank Walter Lunsmann for providing the finite element code used in the numerical simulations.

References

Bairstow, L., Cave, B. M. & Lang, E. D. 1922 The two-dimensional slow motion of viscous fluids. *Proc. R. Soc. Lond.* A **100**, 394–413.

Bairstow, L., Cave, B. M. & Lang, E. D. 1923 The resistance of a cylinder moving in a viscous fluid. *Phil. Trans. R. Soc. Lond.* A **223**, 383–433.

Binding, D. M., Walters, K., Dheur, J. & Crochet, M. J. 1987 Interfacial effects in the flow of viscous and elasticoviscous liquids. *Phil. Trans. R. Soc. Lond.* A **323**, 449–469.

Bird, R. B., Armstrong, R. C. & Hassager, O. 1987*a* *Dynamics of polymeric liquids*, vol. 1 (Fluid mechanics), 2nd edn. New York: Wiley Interscience.

Bird, R. B., Curtiss, C. F., Armstrong, R. C. & Hassager, O. 1987*b* *Dynamics of polymeric liquids*, vol. 2 (Kinetic theory), 2nd edn. New York: Wiley Interscience.

Bisgaard, C. 1983 Velocity fields around spheres and bubbles investigated by laser-Doppler anemometry. *J. non-newtonian Fluid Mech.* **12**, 283–302.

Boger, D. V. 1977 A highly elastic constant-viscosity fluid. *J. non-newtonian Fluid Mech.* **3**, 87–91.

Boger, D. V. 1987 Viscoelastic flows through contractions. *A. Rev. Fluid Mech.* **19**, 157–182.

Boger, D. V., Hur, D. U. & Binnington, R. J. 1986 Further observations of elastic effects in tubular entry flows. *J. non-newtonian Fluid Mech.* **20**, 31–49.

Broadbent, J. M. & Mena, B. 1974 Slow flow of an elastico-viscous fluid past cylinders and spheres. *Chem. Engng J.* **8**, 11–19.

Cable, P. J. & Boger, D. V. 1978 A comprehensive experimental investigation of tubular entry flow of viscoelastic fluids: part 2, the velocity field in stable flow. *A.I.Ch.E. Jl* **24**, 882–999.

Carew, E. O. A. & Townsend, P. 1991 Slow visco-elastic flow past a cylinder in a rectangular channel. *Rheol. Acta* **20**, 58–64.

Caswell, B. & Schwarz, W. H. 1962 The creeping motion of a non-newtonian fluid past a sphere. *J. Fluid Mech.* **13**, 417–426.

Chiba, K., Sakatani, T. & Nakamura, K. 1990 Anomalous flow patterns in viscoelastic entry flow through a planar contraction. *J. non-newtonian Fluid Mech.* **36**, 193–203.

Chiba, K., Tanaka, S. & Nakamura, K. 1992 The structure of anomalous entry flow patterns through a planar contraction. *J. non-newtonian Fluid Mech.* **42**, 315–322.

Chilcott, M. D. & Rallison, J. M. 1988 Creeping flow of dilute polymer solutions past cylinders and spheres. *J. non-newtonian Fluid Mech.* **29**, 381–432.

Chmielewski, C., Nichols, K. L. & Jayaraman, K. 1990 A comparison of the drag coefficients of spheres translating in corn-syrup-based and polybutene-based Boger fluids. *J. non-newtonian Fluid Mech.* **35**, 37–49.

Coates, P. J., Armstrong, R. C. & Brown, R. A. 1992 Calculation of steady-state viscoelastic flow through axisymmetric contractions with the EEME formulation. *J. non-newtonian Fluid Mech.* **42**, 141–188.

Cochrane, T., Walters, K. & Webster, M. F. 1981 On newtonian and non-newtonian flow in complex geometries. *Phil. Trans. R. Soc. Lond.* A **301**, 163–181.

Cressely, R. & Hocquart, R. 1980 Birefringence d'écoulement localisée induite a l'arriere d'obstacles. *Optica Acta* **27**, 699–711.

PHILOSOPHICAL TRANSACTIONS OF THE ROYAL SOCIETY A MATHEMATICAL, PHYSICAL & ENGINEERING SCIENCES

Crochet, M. J. 1988 Numerical simulation of highly viscoelastic flows. In *Proc. Xth Int. Congr. on Rheology* (ed. P. H. T. Uhlherr), vol. 1, pp. 19–24. Sydney: Monash University Press.

Crochet, M. J. 1989 Numerical simulation of viscoelastic flow: a review. *Rubber Chem. Tech.* (*Rubber Rev.*) **62**, 426–455.

Delvaux, V. & Crochet, M. J. 1990 Numerical prediction of anomalous transport properties in viscoelastic flow. *J. non-newtonian Fluid Mech.* **37**, 297–315.

Dhahir, S. A. & Walters, K. 1989 On non-newtonian flow past a cylinder in a confined flow. *J. Rheol.* **33**, 781–804.

Georgiou, G., Momani, S., Crochet, M. J. & Walters, K. 1991 Newtonian and non-newtonian flow in a channel obstructed by an antisymmetric array of cylinders. *J. non-newtonian Fluid Mech.* **39**, 231–260.

Giesekus, H. 1972 On instabilities in Poiseuille and Couette flows of viscoelastic fluids. In *Prog. Heat and Mass Transfer*, vol. 5 (ed. W. R. Schowalter, A. V. Luikov, W. J. Minkowycz & N. H. Afgan), p. 187–193. New York: Pergamon Press.

Harlen, O. G. 1990 High-Deborah-number flow of a dilute polymer solution past a sphere falling along the axis of a cylindrical tube. *J. non-newtonian Fluid Mech.* **37**, 157–173.

Hassager, O. 1988 Working group on numerical techniques. *J. non-newtonian Fluid Mech.* **29**, 2–5.

Hu, H. & Joseph, D. D. 1990 Numerical simulation of viscoelastic flow past a cylinder. *J. non-newtonian Fluid Mech.* **37**, 347–377.

James, D. F. & Acosta, A. J. 1970 The laminar flow of dilute polymer solutions around circular cylinders. *J. Fluid Mech.* **42**, 269–288.

Joo, Y. L. & Shaqfeh, E. S. G. 1991 A purely elastic instability in Dean and Taylor–Dean flow. *Phys. Fluids* A **4**, 524–543.

Joseph, D. D. & Saut, J. C. 1986 Change of type and loss of evolution in the flow of viscoelastic fluids. *J. non-newtonian Fluid Mech.* **20**, 117–141.

Keunings, R. 1987 Simulation of viscoelastic fluid flow. In *Fundamentals of computer modeling for polymer processing* (ed. C. L. Tucker III). Berlin: Carl Hanser Verlag.

Kim, B. K. & Telionis, D. P. 1989 The effect of polymer additives on laminar separation. *Phys. Fluids* A **1**, 267–273.

Koniuta, A., Adler, P. M. & Piau, J.-M. 1980 Flow of dilute polymer solutions around circular cylinders. *J. non-newtonian Fluid Mech.* **7**, 101–106.

Lamb, H. 1932 *Hydrodynamics*, 6th edn. Cambridge University Press.

Larson, R. G. 1989 Taylor–Couette stability analysis for a Doi–Edwards fluid. *Rheol. Acta* **28**, 504–510.

Larson, R. G. 1992 Instabilities in viscoelastic flows. *Rheol. Acta.* **31**, 213–263.

Larson, R. G., Shaqfeh, E. S. G. & Muller, S. J. 1990 A purely elastic instability in Taylor–Couette flow. *J. Fluid Mech.* **218**, 573–600.

Leslie, F. M. & Tanner, R. I. 1961 The slow flow of a viscoelastic liquid past a sphere. *Q. Jl Mech. appl. Math.* **14**, 36–48.

Lunsmann, W. J. 1991 Finite element calculations with viscoelastic fluid models of steady flow past a sphere. M.Sc. thesis. Massachusetts Institute of Technology, Boston, Massachusetts, U.S.A.

Lunsmann, W. J., Gnieser, L., Brown, R. A. & Armstrong, R. C. 1993 Finite element analysis of steady viscoelastic flow around a sphere: calculations with constant viscosity models. *J. non-newtonian Fluid Mech.* (In the press.)

Maalouf, A. & Sigli, D. 1984 Effects of body shape and viscoelasticity on the slow flow around an obstacle. *Rheol. Acta* **23**, 497–507.

Magda, J. J. & Larson, R. G. 1988 A transition occurring in ideal elastic liquids during shear flow. *J. non-newtonian Fluid Mech.* **30**, 1–19.

Magda, J. J., Lou, J., Baek, S.-G. & DeVries, K. L. 1991 Second normal stress difference of a Boger fluid. *Polymer* **32**, 2000–2009.

Manero, O. & Mena, B. 1981 On the slow flow of viscoelastic liquids past a circular cylinder. *J. non-newtonian Fluid Mech.* **9**, 379–387.

PHILOSOPHICAL TRANSACTIONS OF THE ROYAL SOCIETY A MATHEMATICAL, PHYSICAL & ENGINEERING SCIENCES

McKinley, G. H. 1991 The nonlinear dynamics of viscolastic flow in complex geometries. Ph.D. thesis, Massachusetts Institute of Technology, Boston, Massachusetts, U.S.A.

McKinley, G. H., Armstrong, R. C. & Brown, R. A. 1992 LDV measurements of viscoelastic flow instabilities in the wake of confined circular cylinders. In *Proc. XIth Int. Congr. on Rheology* (ed. P. Moldenaers), vol. 1, pp. 198–200. Brussels: Elsevier.

McKinley, G. H., Byars, J. A., Brown, R. A. & Armstrong, R. C. 1991 Observations on the elastic instability in cone-and-plate and parallel-plate flows of a polyisobutylene Boger fluid. *J. non-newtonian Fluid Mech.* **40**, 201–229.

McKinley, G. H., Raiford, W. P., Brown, R. A. & Armstrong, R. C. 1991 Nonlinear dynamics of viscoelastic flow in axisymmetric abrupt contractions. *J. Fluid Mech.* **223**, 411–456.

Mead, D. W. 1987 Ph.D. thesis, Cambridge University, U.K.

Mena, B. & Caswell, B. 1974 Slow flow of an elastic-viscous fluid past an immersed body. *J. chem. Engng* **8**, 125–134.

Mizushina, T. & Usui, H. 1975 Transport phenomena of viscoelastic fluid in cross flow around a circular cylinder. *J. chem. Engng Japan* **8**, 393–398.

Muller, S. J., Larson, R. G. & Shaqfeh, E. S. G. 1989 A purely elastic transition in Taylor–Couette flow. *Rheol. Acta* **28**, 499–503.

Northey, P. J., Armstrong, R. C. & Brown, R. A. 1990 Finite-element calculation of time-dependent two-dimensional viscoelastic flow with the EEME formulation. *J. non-newtonian Fluid Mech.* **36**, 109–133.

Northey, P. J., Armstrong, R. C. & Brown, R. A. 1992 Finite-amplitude, time-periodic states in viscoelastic Taylor–Couette flow described by the UCM model. *J. non-newtonian Fluid Mech.* **42**, 117–139.

Oldroyd, J. G. 1950 On the formulation of rheological equations of state. *Proc. R. Soc. Lond.* A **200**, 523–541.

Pearson, J. R. A. 1985 *Mechanics of polymer processing*. London: Elsevier.

Petrie, C. J. S. & Denn, M. M. 1976 Instabilities in polymer processing. *A.I.Ch.E. Jl* **22**, 209–235.

Pilate, G. & Crochet, M. J. 1977 Plane flow of a second-order fluid past submerged boundaries. *J. non-newtonian Fluid Mech.* **2**, 323–341.

Quinzani, L. M., McKinley, G. H., Brown, R. A. & Armstrong, R. C. 1990 Modeling the rheology of polyisobutylene solutions. *J. Rheol.* **34**, 705–748.

Rajagopalan, D. R., Byars, J. A., Armstrong, R. C., Brown, R. A., Lee, J. S. & Fuller, G. G. 1992 Comparison of numerical simulations and birefringence measurements in viscoelastic flow between eccentric rotating cylinders. *J. Rheol.* **36**, 1349–1375.

Skartsis, L., Khomami, B. & Kardos, J. L. 1992 Polymeric flow through fibrous media. *J. Rheol.* **36**, 589–620.

Smith, K. A., Merrill, E. W., Mickley, H. S. & Virk, P. S. 1967 Anomalous pitot tube and hot film measurements in dilute polymer solutions. *Chem. Engng Sci.* **22**, 619–626.

Tadmor, Z. & Gogos, C. G. 1979 *Principles of polymer processing*. New York: Wiley Interscience.

Tirtaatmadja, V., Uhlherr, P. H. T. & Sridhar, T. 1990 Creeping motion of spheres in fluid M1. *J. non-newtonian Fluid Mech.* **35**, 327–337.

Tomita, Y. & Takahashi, T. 1988 An anomalous phenomenon occurring in the flow of viscoelastic fluids out of ducts. *Rheol. Acta* **27**, 523–530.

Townsend, P. 1980 A numerical simulation of newtonian and viscoelastic flow past stationary and rotating cylinders. *J. non-newtonian Fluid Mech.* **6**, 219–243.

Townsend, P. 1984 On the numerical simulation of two-dimensional time-dependent flows of Oldroyd fluids. Part 1. Basic method and preliminary results. *J. non-newtonian Fluid Mech.* **14**, 265–278.

Ultmann, J. S. & Denn, M. M. 1971 Slow viscoelastic flow past submerged objects. *J. chem. Engng* **2**, 81–89.

Usui, H., Shibata, T. & Sano, Y. 1980 Kármán vortex behind a circular cylinder in dilute polymer solutions. *Chem. Engng J. Japan* **13**, 77–79.

Walters, K. 1985 Overview of macroscopic viscoelastic flow. In *Viscoelasticity and rheology* (ed. A. S. Lodge, M. Renardy & J. A. Nohel), pp. 47–55. Orlando: Academic Press.

PHILOSOPHICAL TRANSACTIONS OF THE ROYAL SOCIETY A MATHEMATICAL, PHYSICAL & ENGINEERING SCIENCES

Walters, K. & Tanner, R. I. 1992 The motion of a sphere through an elastic liquid. In *Transport processes in bubbles, drops and particles* (ed. R. P. Chhabra & D. De Kee), pp. 73–86. New York: Hemisphere.

Walters, K. & Webster, M. F. 1982 On dominating elastico-viscous response in some complex flows. *Phil. Trans. R. Soc. Lond.* A **308**, 199–218.

Zana, E., Tiefenbruck, G. & Leal, L. G. 1975 A note on the creeping motion of a viscoelastic fluid past a sphere. *Rheol. Acta* **14**, 891–898.

Received 7 August 1992; accepted 7 October 1992

PHILOSOPHICAL TRANSACTIONS OF THE ROYAL SOCIETY A MATHEMATICAL, PHYSICAL & ENGINEERING SCIENCES

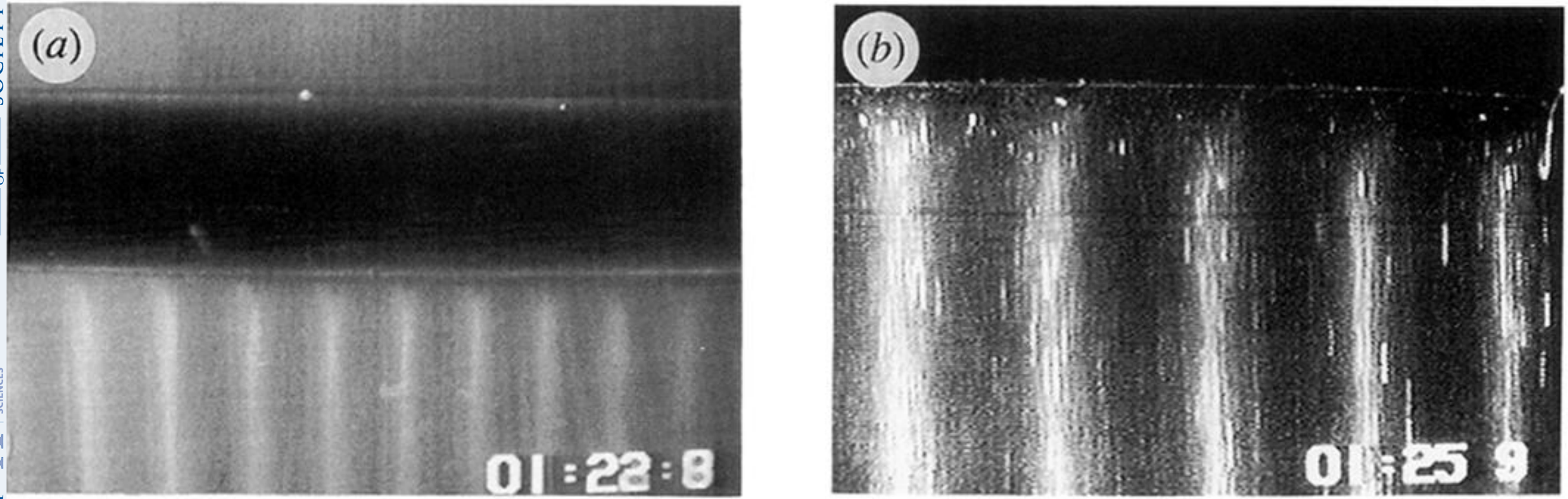

Figure 14. The elastic wake instability at $De = 2.48$, $Re = 0.028$. (*a*) Video-imaging of the flow shows the formation of a cellular structure in the downstream wake that extends along the length of the cylinder; (*b*) higher magnification image close to the downstream stagnation point shows that the velocity in the cylinder wake is three-dimensional with a v_x component parallel to the cylinder axis.